Brune, S. (2014): Evolution of stress and fault patterns in oblique rift systems: 3-D numerical lithospheric-scale experiments from rift to breakup. - *Geochemistry Geophysics Geosystems (G3)*, *15*, 8, p. 3392-3415.

DOI: http://doi.org/10.1002/2014GC005446

AGU PUBLICATIONS

Geochemistry, Geophysics, Geosystems

RESEARCH ARTICLE
10.1002/2014GC005446

Key Points:
- 3-D numerical rift models are conducted covering the entire obliquity spectrum
- A constant extension direction can generate multiphase fault orientations
- A characteristic evolution of fault patterns from rift to breakup is identified

Supporting Information:
- Readme
- Supplementary Figures S1–S5
- Alpha A1–A7

Correspondence to:
S. Brune,
brune@gfz-potsdam.de

Citation:
Brune, S. (2014), Evolution of stress and fault patterns in oblique rift systems: 3-D numerical lithospheric-scale experiments from rift to breakup, *Geochem. Geophys. Geosyst.*, *15*, 3392–3415, doi:10.1002/2014GC005446.

Received 5 JUN 2014
Accepted 17 JUL 2014
Accepted article online 22 JUL 2014
Published online 21 AUG 2014

Evolution of stress and fault patterns in oblique rift systems: 3-D numerical lithospheric-scale experiments from rift to breakup

Sascha Brune[1,2]

[1]Helmholtz Centre Potsdam, GFZ German Research Centre for Geosciences, Geodynamic Modelling Section, Potsdam, Germany, [2]School of Geosciences, University of Sydney, EarthByte Group, Sydney, Australia

Abstract Rifting involves complex normal faulting that is controlled by extension direction, reactivation of prerift structures, sedimentation, and dyke dynamics. The relative impact of these factors on the observed fault pattern, however, is difficult to deduce from field-based studies alone. This study provides insight in crustal stress patterns and fault orientations by employing a laterally homogeneous, 3-D rift setup with constant extension velocity. The presented numerical forward experiments cover the whole spectrum of oblique extension. They are conducted using an elastoviscoplastic finite element model and involve crustal and mantle layers accounting for self-consistent necking of the lithosphere. Despite recent advances, 3-D numerical experiments still require relatively coarse resolution so that individual faults are poorly resolved. This issue is addressed by applying a post processing method that identifies the stress regime and preferred fault azimuth at each surface element. The simple model setup results in a surprising variety of fault orientations that are solely caused by the three-dimensionality of oblique rift systems. Depending on rift obliquity, these orientations can be grouped in terms of rift-parallel, extension-orthogonal, and intermediate normal fault directions as well as strike-slip faults. While results compare well with analog rift models of low to moderate obliquity, new insight is gained in advanced rift stages and highly oblique settings. Individual fault populations are activated in a characteristic multiphase evolution driven by lateral density variations of the evolving rift system. In natural rift systems, this pattern might be modified by additional heterogeneities, surface processes, and dyke dynamics.

1. Introduction

Oblique extension takes place when the relative velocity of two diverging plates is oblique to the rift trend (Figure 1). It occurs currently in both continental and oceanic settings such as the Ethiopian Rift System [*Corti*, 2008], the Malawi Rift [*Chorowicz and Sorlien*, 1992], the Aegean Rift [*Agostini et al*., 2010], the Reykjanes and Mohns ridge [*Dauteuil and Brun*, 1993], and the South West Indian Ridge [*Dick et al*., 2003; *Montési et al*., 2011]. During Pangaea fragmentation, oblique rifting often lead to continental breakup as for the separation of Africa and South America [*Nürnberg and Müller*, 1991; *Torsvik et al*., 2009; *Moulin et al*., 2010; *Heine and Brune*, 2014], Madagascar and Africa [*de Wit*, 2003], Madagascar and India [*Storey et al*., 1995], Sri Lanka and South India from Antarctica [*Gaina et al*., 2007], and Antarctica and Australia [*Whittaker et al*., 2007; *Williams et al*., 2011]. Oblique rifting took place during the formation of the Gulf of Aden [*Bellahsen et al*., 2003; *Brune and Autin*, 2013], the Gulf of California [*Lizarralde et al*., 2007; *Bennett and Oskin*, 2014] as well as in the North Atlantic upon formation of the Davis Strait [*Suckro et al*., 2012; *Hosseinpour et al*., 2013], and the Fram Strait [*Engen et al*., 2008].

Oblique rift systems exhibit a complex spatiotemporal fault evolution that may be due to activation of inherited crustal heterogeneities or anisotropies [*Smith and Mosley*, 1993; *Ring*, 1994], magmatic intrusions [*Buck*, 2006; *Rooney et al*., 2014], rotations of the extension direction [*Strecker et al*., 1990; *Ring*, 1994; *Bonini et al*., 1997], and interaction of tectonics with sedimentation [*Bialas and Buck*, 2009; *Dorsey*, 2010].

In order to elucidate the structures and evolution of oblique extensional systems analog modeling has been successful on both crustal and lithospheric scale: (i) Models on crustal scale simulate rifting via a brittle crust that is underlain by a basal zone of extension including an oblique velocity discontinuity [*Withjack and Jamison*, 1986; *Tron and Brun*, 1991; *McClay and White*, 1995; *Clifton et al*., 2000; *Mart and*

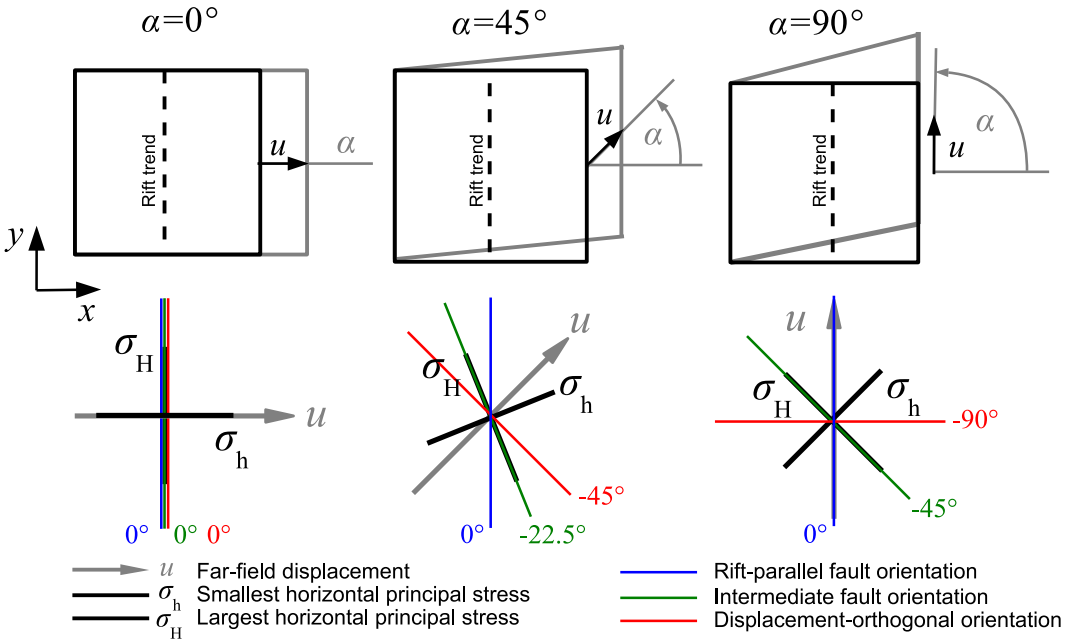

Figure 1. Geometry of oblique rifting. The angle of obliquity α is the angle between the far field extension and the rift normal; it is 0° for pure extension and 90° for large-scale simple shear motion. With increasing obliquity, the stress field and the associated fault orientations rotate to the indicated azimuth. The "intermediate" fault orientation is defined to lie in the middle between rift-parallel and extension-orthogonal direction.

Dauteuil, 2000; *Corti et al*., 2001, 2003]. With this approach, crustal strain patterns are investigated independently from mantle deformation. Hence, lithospheric necking and associated isostatic balancing are not accounted for which limits the model applicability to the initial rift stage. (ii) Recently, lithospheric-scale laboratory experiments have been conducted that incorporated thinning of the lithosphere and its influence on crustal fault patterns [*Sokoutis et al*., 2007; *Corti*, 2008; *Agostini et al*., 2009; *Autin et al*., 2010; *Corti*, 2012].

A main feature of all analog experiments with moderate obliquity ($\alpha < \sim 60°$, where α is the angle of obliquity measured between rift normal and direction of extension) is that the principal strain directions are generally not parallel to the direction of relative movement between the extending plates. *Withjack and Jamison* [1986] showed that for low amounts of bulk extension, the fault orientation within the rift trends halfway between the extensional-orthogonal direction and the rift trend (Figure 1). They also addressed the occurrence of strike-slip faults by showing that for crustal-scale models with low to moderate obliquity, the vertical principal stress σ_v is identified with σ_1 and the largest horizontal stress σ_H with σ_2. With higher obliquity, however, the difference between σ_v and σ_H decreases until σ_H becomes the largest principal stress. In this case, both σ_1 and σ_3 are horizontal and strike-slip deformation takes place. Using infinitesimal strain theory, *Withjack and Jamison* [1986] calculated that a critical angle of obliquity $\alpha_{crit} = 71°$ has to be exceeded in order for strike-slip faulting to occur. For larger amounts of bulk extension, rift-parallel and extension-orthogonal fault populations have been observed in lithospheric-scale models [*Agostini et al*., 2009; *Autin et al*., 2010].

Reproducing realistic, scalable rheologies, adequate boundary conditions and especially the introduction of temperature-dependent viscosity pose severe problems in laboratory experiments. Many numerical models, however, include these features and were used to study rifting in a 2-D setting [e.g., *Zuber and Parmentier*, 1986; *Braun and Beaumont*, 1989; *Bassi*, 1991; *Buck*, 1991; *Burov and Cloetingh*, 1997; *Lavier et al*., 2000; *Behn et al*., 2002; *Van Wijk and Cloetingh*, 2002; *Huismans and Beaumont*, 2003; *Pérez-Gussinyé et al*., 2006; *Lavier and Manatschal*, 2006; *Regenauer-Lieb et al*., 2006; *Buiter et al*., 2008; *Petersen et al*., 2010; *Huismans and Beaumont*, 2011; *Rey et al*., 2011; *Choi and Buck*, 2012; *Liao and Gerya*, 2014; *Brune et al*., 2014]. However, computational models of oblique rifting necessitate 3-D calculations which severely limits the model resolutions and constitutes a fundamental constraint to present-day numerical

models. Addressing only crustal deformation of a 3-D rift system strongly limits the computational effort which allows for comparatively higher resolution [*Katzman et al*., 1995; *Allken et al*., 2011, 2012]; however, it is valid only during the initial rift stage, where the influence of a deforming mantle lithosphere can be neglected. This disadvantage is overcome by 3-D numerical experiments that involve both crust and mantle layers [*Dunbar and Sawyer*, 1996; *van Wijk and Blackman*, 2005; *van Wijk*, 2005; *Gac and Geoffroy*, 2009; *Gerya*, 2010; *Le Pourhiet et al*., 2012; *Brune et al*., 2013; *Gerya*, 2013; *Heine and Brune*, 2014; *Le Pourhiet et al*., 2014].

In this paper, I investigate the structures of oblique rift systems by means of a lithospheric-scale numerical model that includes elastoviscoplastic rheology with laboratory-based flow laws for temperature and pressure-dependent viscosity. The presented models address the whole extensional process from initial fault coalescence to breakup. This analysis involves the conventional approach to compute and interpret shear zone patterns in terms of strain-rate and plastic strain. Additionally, a recently developed stress interpretation technique is used [*Brune and Autin*, 2013] that allows the evaluation of fault patterns on a sub-shear zone level.

2. Model Description

2.1. Numerical Model Setup

The numerical 3-D rift setup involves laterally homogeneous material layers without inherited structures, constant extension velocity, and direction. The thermomechanically coupled conservation equations of momentum, energy, and mass are solved using the implicit, finite element code SLIM3D (Semi-Lagrangian Implicit Model for 3-D). A detailed description of the numerical techniques is given in *Popov and Sobolev* [2008].

The presented models comprise a segment of the Earth that measures 249 km times 249 km horizontally and 120 km vertically (Figure 2). It is divided in 275,560 cubic elements with a length of 3 km. At the left and right model side, a velocity of 5 mm/yr is prescribed, resulting in a full extension velocity of 10 mm/yr. Hence, an extension of e.g., 200 km is reached after 20 My model time. The angle of obliquity α is defined as the angle between the boundary velocity vector and the boundary normal. A different obliquity is applied during each model run in order to scan from orthogonal extension ($\alpha=0^\circ$) over oblique rifting to strike-slip motion ($\alpha=90^\circ$). Note that the width of the model domain stays the same during extension, so that there is outflow of material across the left and right model boundaries. The code features a free surface at the top boundary, while at the bottom boundary isostatic equilibrium is realized by means of the Winkler foundation, where inflow of material is accounted for during remeshing. An important feature of the model is the periodic boundary condition that connects the front and back sides so that an effectively infinitely long rift zone is realized. In order to localize deformation to the model center, a small elongate temperature heterogeneity is applied in the middle of the prospective rift (Figure 2a). This approach effectively mimics a small amount of lithospheric thinning and importantly, it does not prescribe any fault structures at the surface.

The model comprises four distinct rheological layers, namely a 20 km thick upper crust featuring wet quartzite properties [*Gleason and Tullis*, 1995], a lower crust of 15 km thickness with granulite rheology [*Wilks and Carter*, 1990], a 45 km thick layer of lithospheric mantle with dry olivine rheology [*Hirth and Kohlstedt*, 2003], and an asthenospheric layer that is represented by the flow law of wet (i.e., 500 ppm H/Si) olivine below 90 km depth [*Hirth and Kohlstedt*, 2003]. A list of all thermomechanical parameters can be found in Table 1.

Thermomechanical weakening affects the model evolution by three mechanisms: (i) Friction softening: Crustal fault strength is successively reduced by continued deformation within a fault zone [*Zoback et al*., 1987; *Provost and Houston*, 2003]. This process is introduced using a strain-dependent effective friction coefficient that decreases linearly from 0.6 to 0.06 for plastic strains between 0 and 1, while it remains constant at 0.06 for plastic strains larger than 1. This corresponds to a decrease of the effective friction angle from 31° to 3.5°. (ii) Shear heating: An increased rate of deformation leads to heat production which lowers the effective viscosity. A smaller viscosity attracts deformation and thus increases the strain rate. (iii) Dislocation creep involves a power law dependency between strain rate and stress that allows localization in terms of viscosity reduction.

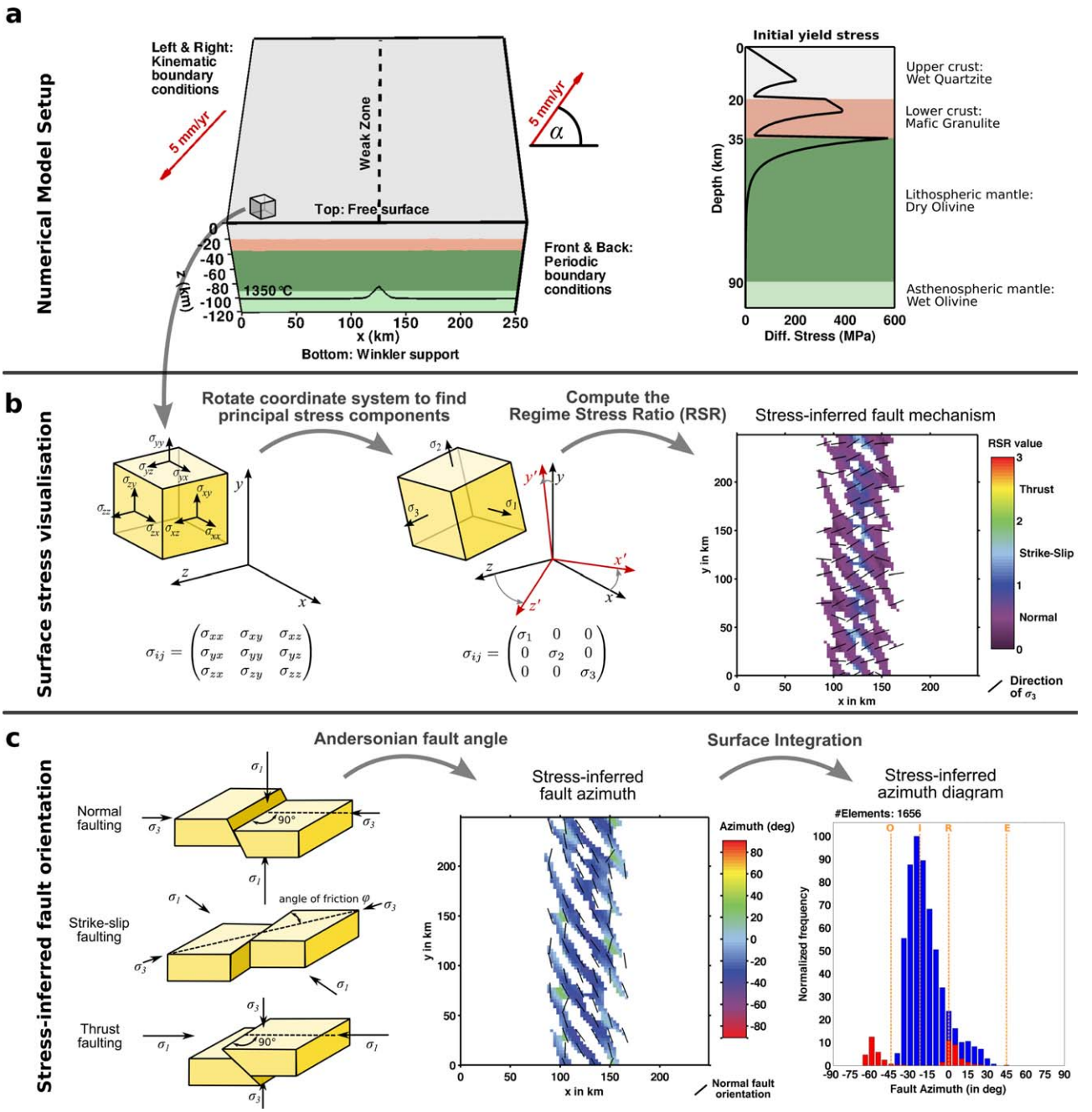

Figure 2. Model setup. (a) Extensional velocities are prescribed at the boundaries in *x* direction. Periodic boundary conditions in *y* direction realize an in principle infinitely long rift zone. A thermally weak zone initializes rifting by effectively introducing a small amount of lithospheric necking. (b) The stress tensor is used to calculate the regime stress ratio (RSR) at each surface element. (c) The optimal fault orientation with respect to the stress field is computed for each surface element and condensed in an azimuth diagram.

2.2. Stress Interpretation Method

In most thermomechanical codes (including SLIM3D), brittle deformation localizes in the form of shear bands with a typical width of few elements. This limits the capabilities of currently relatively coarse 3-D models to reproduce the fault patterns that are visible both in nature and in analog models. However, a great advantage of numerical models is to offer direct access to the stress tensor at any element of the model. Here we exploit this advantage by means of a simple post processing technique that analyzes the stress tensor at the model surface in order to infer stress regime and the optimal orientation of small-scale faults [*Brune and Autin*, 2013]. This method extracts information from the model which is not accessible to

Table 1. Model Parameters

Parameter	Upper Crust	Lower Crust	Strong Mantle	Weak Mantle
Density, ρ (kg m^{-3})	2700	2850	3280	3300
Thermal expansivity, α_T (10^{-5} K^{-1})	2.7	2.7	3.0	3.0
Bulk modulus, K (GPa)	55	63	122	122
Shear modulus, G (GPa)	36	40	74	74
Heat capacity, C_p (J kg^{-1} K^{-1})	1200	1200	1200	1200
Heat conductivity, λ (W K^{-1} m^{-1})	2.5	2.5	3.3	3.3
Radiogenic heat production, A (μW m^{-3})	1.5	0.2	0.0	0.0
Initial friction coefficient, μ (-)	0.6	0.6	0.6	0.6
Cohesion, c (MPa)	5.0	5.0	5.0	5.0
Preexponential constant for diffusion creep, log(B_{Diff}) (Pa^{-1} s^{-1})	-	-	−8.65	−8.65
Activation energy for diffusion creep, E_{Diff} (kJ/mol)	-	-	375	335
Activation volume for diffusion creep, V_{Diff} (cm^{-3}/mol)	-	-	6	4
Preexponential constant for dislocation creep, log(B_{Disloc}) (Pa^{-n}s^{-1})	−28.00	−21.05	−15.56	−15.05
Power law exponent for dislocation creep, n	4.0	4.2	3.5	3.5
Activation energy for dislocation creep, E_{Disloc} (kJ/mol)	223	445	530	480
Activation volume for dislocation creep, V_{Disloc} (cm^{-3}/mol)	0	0	13	10

Dislocation creep parameters for upper crust: wet quartzite [*Gleason and Tullis*, 1995], lower crust: Pikwitonian granulite [*Wilks and Carter*, 1990], lithospheric mantle: dry olivine [*Hirth and Kohlstedt*, 2003], asthenospheric mantle: wet olivine, i.e., 500 ppm H/Si [*Hirth and Kohlstedt*, 2003].

The friction coefficient μ decreases linearly by 90% of the initial value until plastic strain reaches 1, and remains constant for larger strains.

standard visualizations of strain or strain rate and thereby allows a more detailed interpretation of the numerical experiments. It applies the following recipe:

First, the principal stress components, i.e., the eigenvalues σ_1, σ_2, and σ_3 of the stress tensor and the corresponding eigenvectors, are computed at each surface element. The surface stress regime is evaluated in terms of the scalar Regime Stress Ratio (RSR) that indicates extension, strike-slip motion, and compression on a continuous scale [*Simpson*, 1997; *Delvaux et al*., 1997; *Buchmann and Connolly*, 2007; *Hergert and Heidbach*, 2011]. An equivalent alternative method that uses the nondimensional Argand Ratio has been successfully used in analyzing stress states of thin sheet models [*England and McKenzie*, 1982; *Houseman and England*, 1986; *Rey and Houseman*, 2006]. In order to compute the RSR value, the vertical, smallest horizontal, and largest horizontal stress components are used (σ_v, σ_h, and σ_H, respectively) to define the index n

$$n=\left\{\begin{array}{l} 0 \text{ if } \sigma_h < \sigma_H < \sigma_v \text{ (normal faulting)} \\ 1 \text{ if } \sigma_h < \sigma_v < \sigma_H \text{ (strike}-\text{slip faulting)} \\ 2 \text{ if } \sigma_v < \sigma_h < \sigma_H \text{ (thrust faulting)} \end{array}\right\}$$

and the ratio R between smallest and largest differential stress [*Bott*, 1959],

$$R=\left(\frac{\sigma_2-\sigma_3}{\sigma_1-\sigma_3}\right)$$

which allows to compute the RSR value via

$$\text{RSR}=(n+0.5)+(-1)^n(R-0.5)$$

The RSR value maps all possible stress regimes to the interval between 0 and 3. The meaning of the RSR value is illustrated using two examples (Figure 3). The data are drawn from the non-oblique and the highly oblique scenarios of section 3 (α=0° and α=60°, respectively). σ_v, σ_h, and σ_H are measured in the surface element at x = 125 km and y = 125 km. For α=0°, the identification of the principal stress components is obviously $\sigma_1 = \sigma_v$, $\sigma_2 = \sigma_H$, and $\sigma_3 = \sigma_h$ indicating an extensional character of the stress tensor. Even though σ_v and σ_h vary significantly, the ratio R does not change much so that the RSR value remains in the normal faulting domain. The situation changes for α=60°, where σ_1 and σ_2 exchange their identification with σ_v and σ_H which leads from an initially transtensional regime through a strike-slip incursion at 10–14 My to pure extension at 20 My.

Once the stress regime at each element is known, an optimally oriented fault direction can be inferred. Assuming isotropic and homogeneous materials, the standard rules of Andersonian faulting are applied [*Anderson*, 1948] so that extensional (RSR≤1) and compressive (RSR>2) stress regimes generate σ_3-orthogonal and σ_1-orthogonal fault azimuths, respectively. Strike-slip faults occur for 1<RSR≤2 at $\pm\varphi_{eff}$ from σ_1

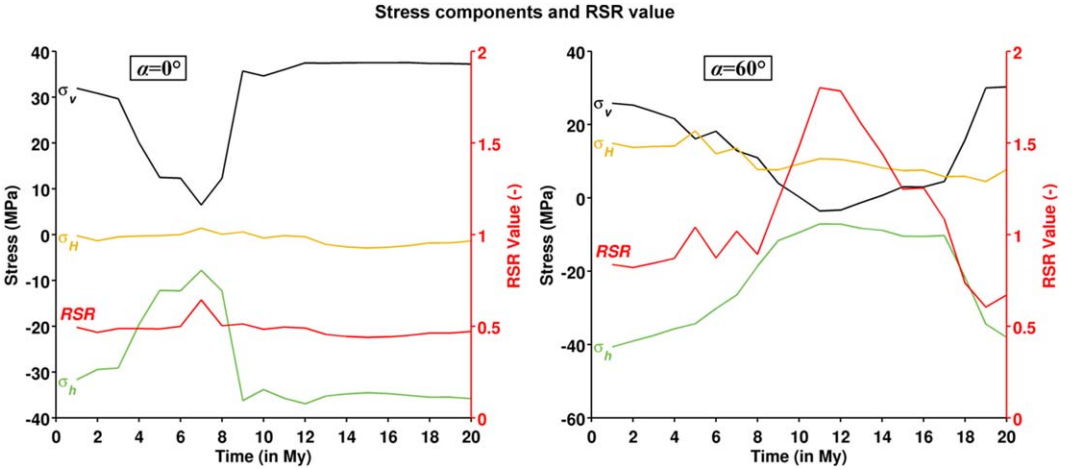

Figure 3. Illustration of the RSR value. The stress regime can be visualized using the RSR value that continuously varies between extension (RSR≤1), strike-slip motion (1<RSR≤2), and compression (RSR>2). Time series of deviatoric stress components are taken at the central coordinates (*x*, *y*) = (125 km, 125 km) of experiments shown in Figures 4 and 8.

(with the effective friction angle $\varphi_{\text{eff}} = 31°$). Note that the stress tensor information alone does not suffice to discriminate between the two strike-slip conjugates (dextral or sinistral) that differ by an azimuth of $2\varphi_{\text{eff}}$. While accounting for both conjugate fault populations, their number is hereafter scaled with a factor of 0.5 so that the overall number of strike-slip elements is not affected.

Azimuth diagrams (Figures 4e–10e) depict the significance of individual fault directions by binning the number of elements within a given azimuth interval. Thus, they can be directly compared to fault length histograms of analog models. Azimuth diagrams are normalized such that the dominant fault orientation is always depicted with a frequency of 100.

By computing optimal fault orientations as a function of local stress state, it is assumed that faults develop in homogeneous, isotropic material. This means that stress-inferred fault orientations only account for the infinitesimal strain field. In reality, the finite strain field involves long-lived faults that might rotate until they deform via oblique slip so that they are not optimally oriented anymore. Obviously, these faults can not be reproduced by this approach. However, a recent study of oblique-spreading oceanic ridges (Southwest Indian, Sheba, Carlsberg, Reykjanes, and Mohns Ridge) compared earthquake focal mechanisms which are markers of infinitesimal strain with normal fault orientations representing the finite strain field [*Fournier and Petit*, 2007]. It was shown that both observations correspond to the same direction of σ_h which implies that normal faults at ridge axes only accommodate a small amount of strain while they are in the zone of active deformation. Further evidence for dominating dip-slip motion of rift faults has been assembled in the Baikal Rift [*Petit et al*., 1996], the Western branch of the East African Rift [*Morley*, 2010], and the Main Ethiopian Rift [*Corti et al*., 2013]. These studies support the hereafter applied assumption of optimally oriented, Andersonian dip-slip faults for oceanic and continental rift systems.

The stress interpretation method allows the computation of fault mechanism and azimuth for any stress tensor, even though the considered element experiences no strain at all. Hence, it is necessary to exclude the quasi-nondeforming region outside the rift zone from the analysis. I restrict my analysis to the zone of tectonic activity, where the strain rate exceeds 10^{-15} s^{-1} (see black contour in Figures 4a–10a). This number is somewhat arbitrary, but the overall results are not affected if the threshold value is changed within the range of reasonable values (see supporting information Figures S4 and S5). Since the extent of the active region (i.e., with strain rate larger than 10^{-15} s^{-1}) varies through time, the overall number of elements that contribute to the analysis changes for each time step and is indicated in the azimuth diagrams (Figures 4e–10e) in the upper left corner (#Elements).

3. Modeling Results

In this section, the general behavior of the numerical models is briefly discussed before individual models are interpreted. The next section relates the first rift stages of the presented models to previously conducted analog models.

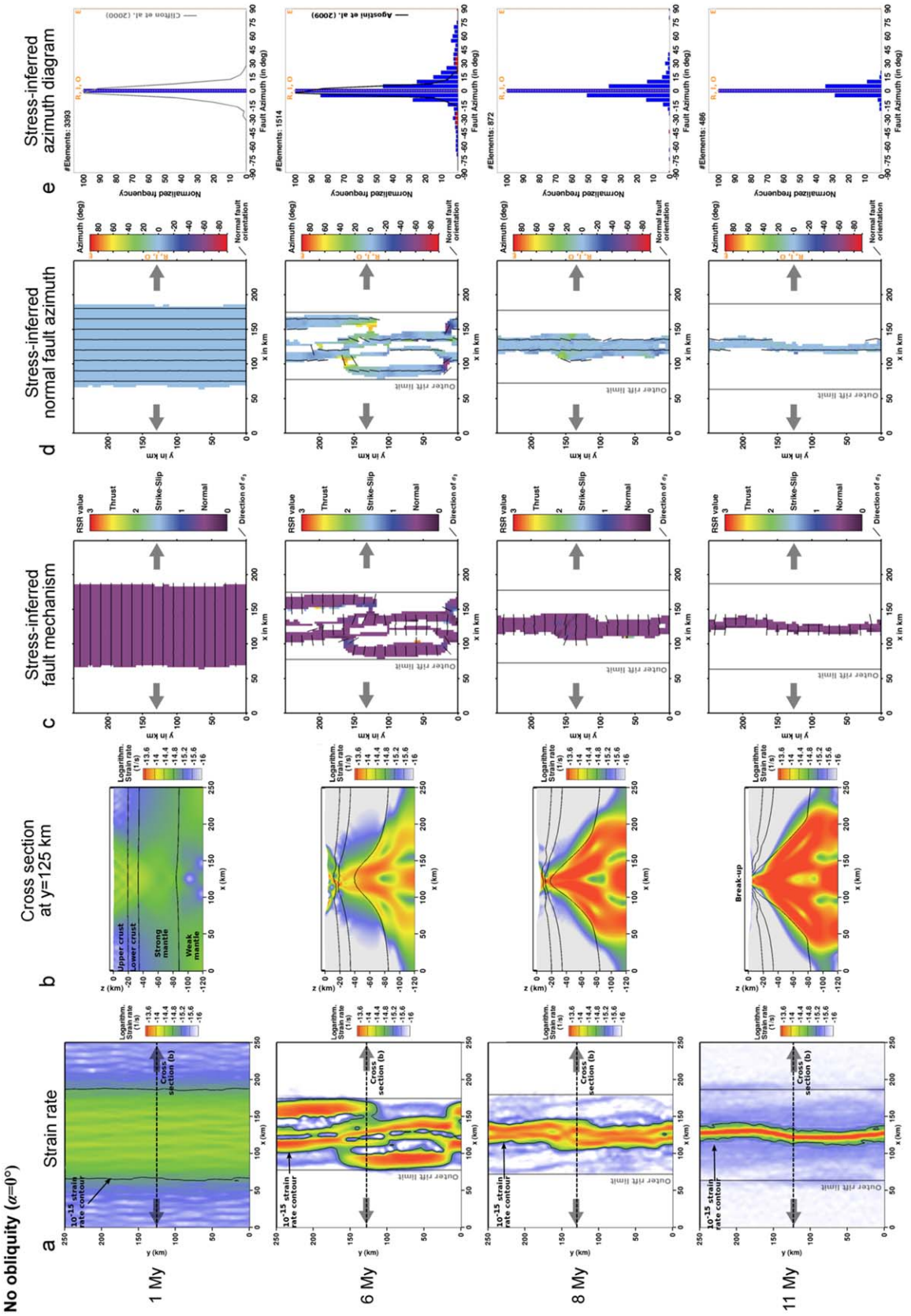

Figure 4. No obliquity (α=0°). (a) Two rift segments with a small offset emerge and unite. (b) The cross section depicts successive lithospheric necking and basinward fault localization. (c) Normal faulting is inferred from the state of stress throughout the experiment. Note that only the active deformation region inside the 10^{-15} s^{-1} strain rate isoline of Figure 4a is used for stress-based evaluation of fault characteristics. (d, e) The normal fault azimuth is 0° except at the rift offset. Abbreviated directions indicate the rift-parallel azimuth (R), intermediate fault orientation (I), extension-orthogonal direction (O), and the direction of extension (E). The number of contributing elements (with a strain rate of 10^{-15} s^{-1} or more) are marked in the upper left corner of each diagram in Figure 4e. The azimuth diagram shows the number of elements that fall within a 5° azimuth interval, while each diagram is normalized to 100%. For comparison, azimuth diagrams of *Clifton et al.* [2000] and *Agostini et al.* [2009] are plotted at 1 and 6 My, respectively. "Outer rift limit" in Figures 4a, 4c, and 4d indicates the moving location of outmost boundary faults as a reference. For a detailed model evolution in 1 My time steps, see supporting information animation A1.

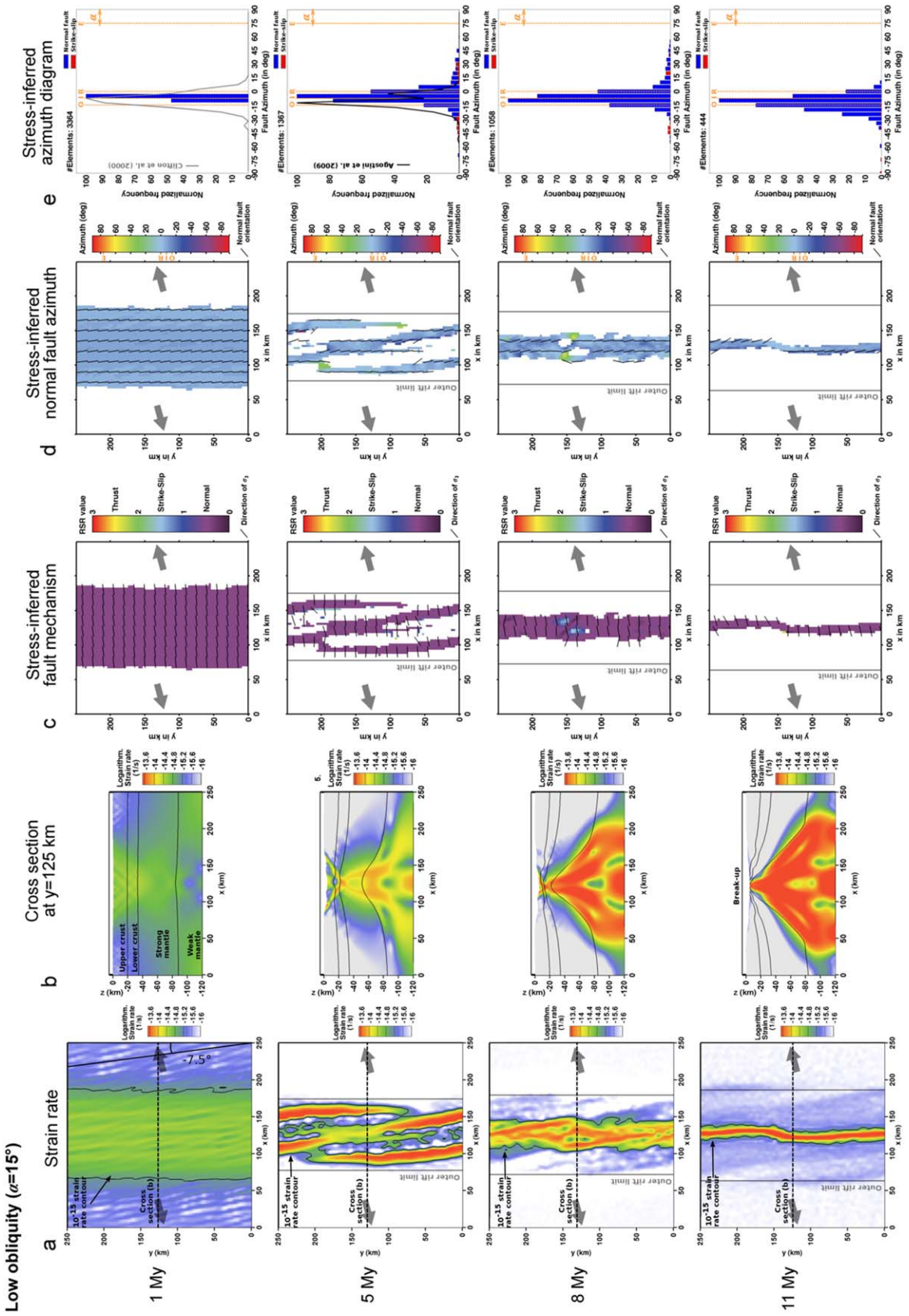

Figure 5. Low obliquity ($\alpha = 15°$). (a) Initial shear zones at 1 My are parallel to the expected shear zone azimuth with intermediate direction. Two en-échelon rift segments form (5 My) and unite (8 My). (b) Cross section showing the degree of lithospheric necking. (c, d, e) Normal faulting dominates the whole model with intermediate azimuth except for the region of the rift offset where azimuths rotate to higher values. Abbreviations are explained in the caption of Figure 4. For a detailed model evolution in 1 My time steps, see supporting information animation A2.

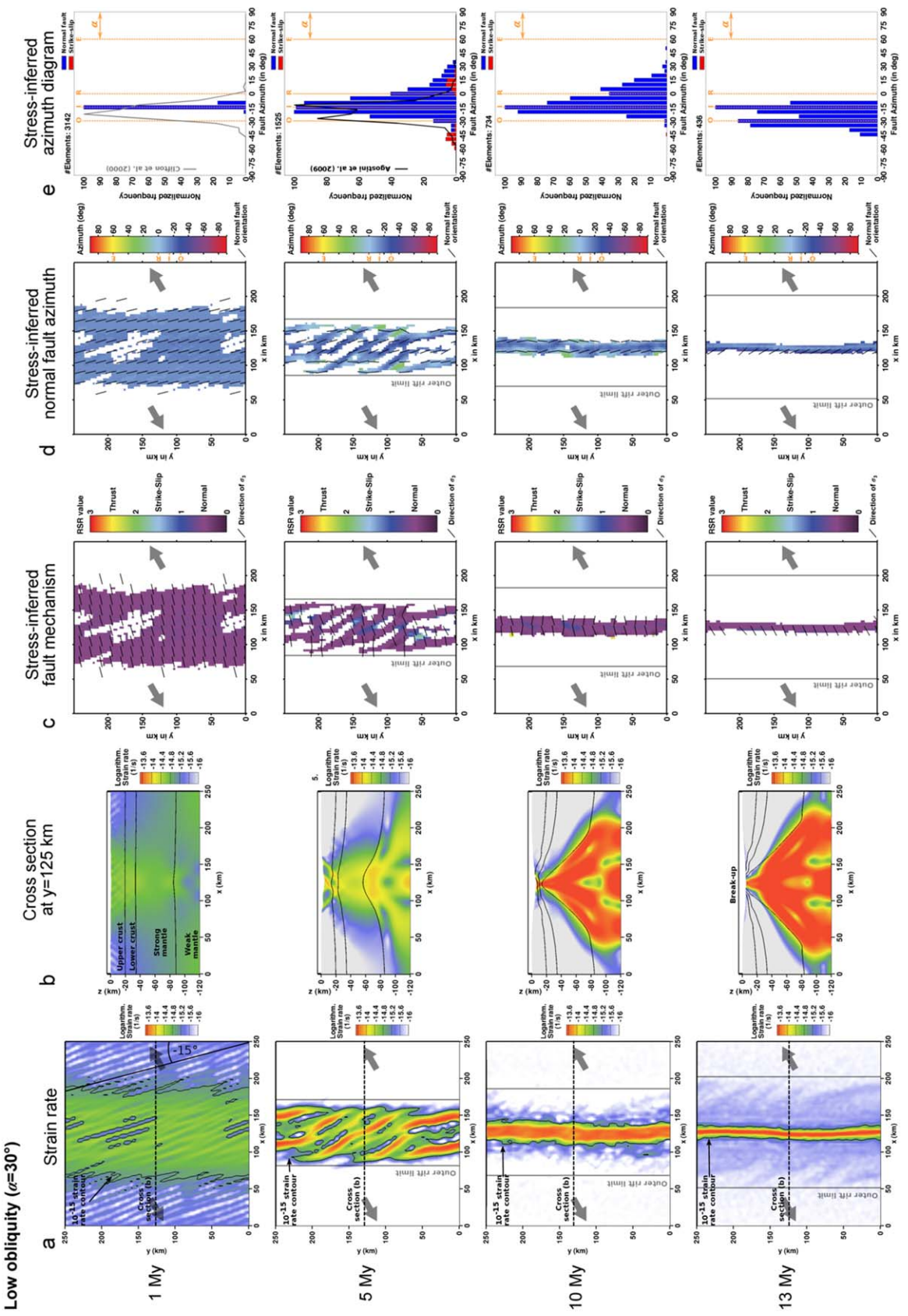

Figure 6. Low obliquity ($\alpha = 30°$). (a) Initial shear zones show an intermediate direction of $-15°$. (b) Cross section showing the degree of lithospheric necking. (c) The stress-inferred fault mechanism is normal except for a short period of strike-slip faulting in the rift center (5 My). (d, e) Stress-inferred normal fault azimuth deviates from intermediate orientation only between individual shear zones where they rotate toward a higher angle. Extension-orthogonal and intermediate fault directions dominate after breakup. Abbreviations are explained in the caption of Figure 4. For a detailed model evolution in 1 My time steps, see supporting information animation A3.

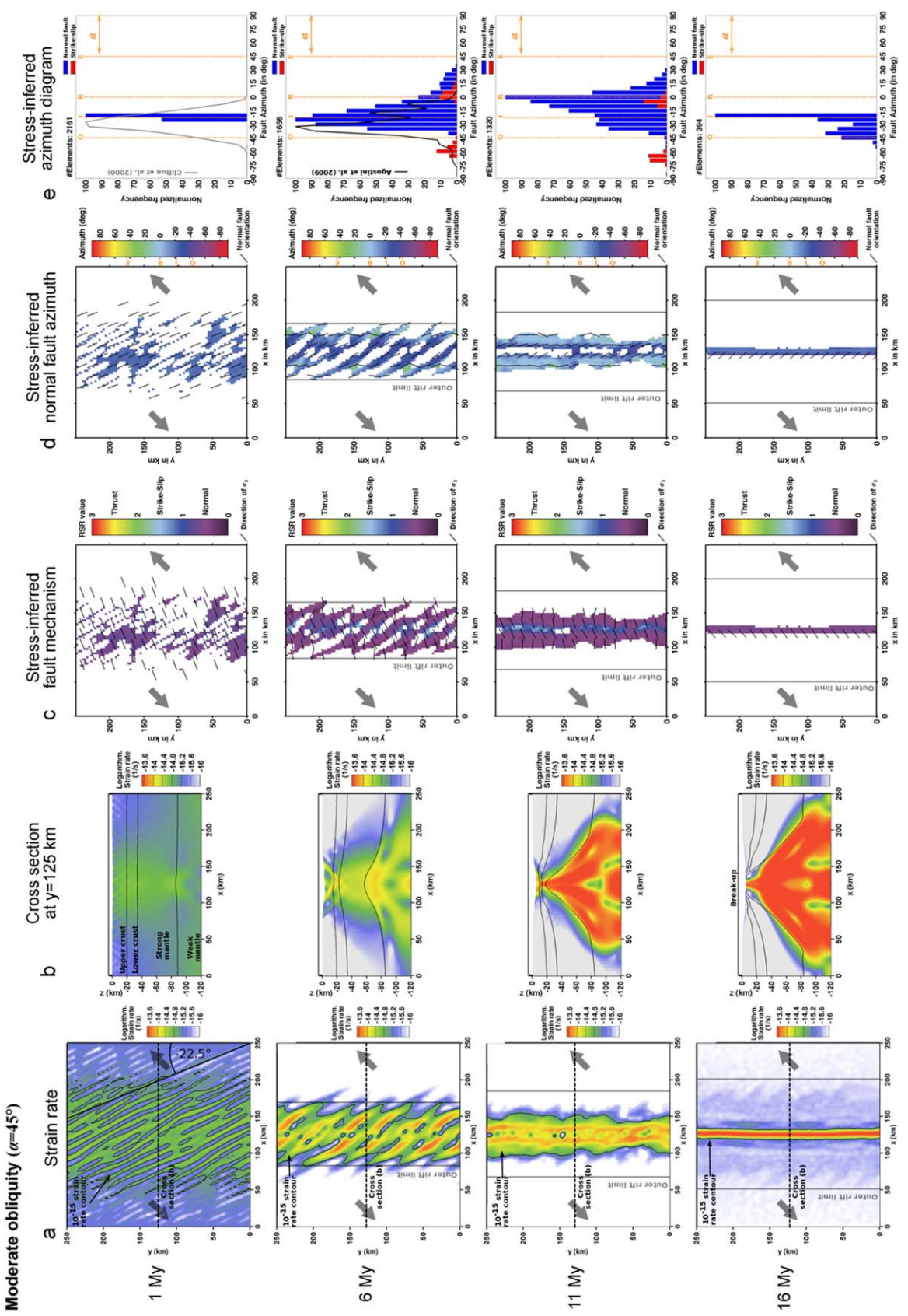

Figure 7. Moderate obliquity (α=45°). (a) Initial shear zones feature intermediate directions before they form a sigmoidal en-échelon pattern. (b) Cross section showing the degree of lithospheric necking. (c, d, e) A strike-slip region exists at 6 and 11 My in the otherwise normal-fault dominated rift. Simultaneously, normal fault azimuths successively shift from intermediate to rift-parallel direction. This shift also coincides with pronounced lithospheric necking in Figure 7b. During and after breakup, intermediate and extension-orthogonal orientations occur. Abbreviations are explained in the caption of Figure 4. For a detailed model evolution in 1 My time steps, see supporting information animation A4.

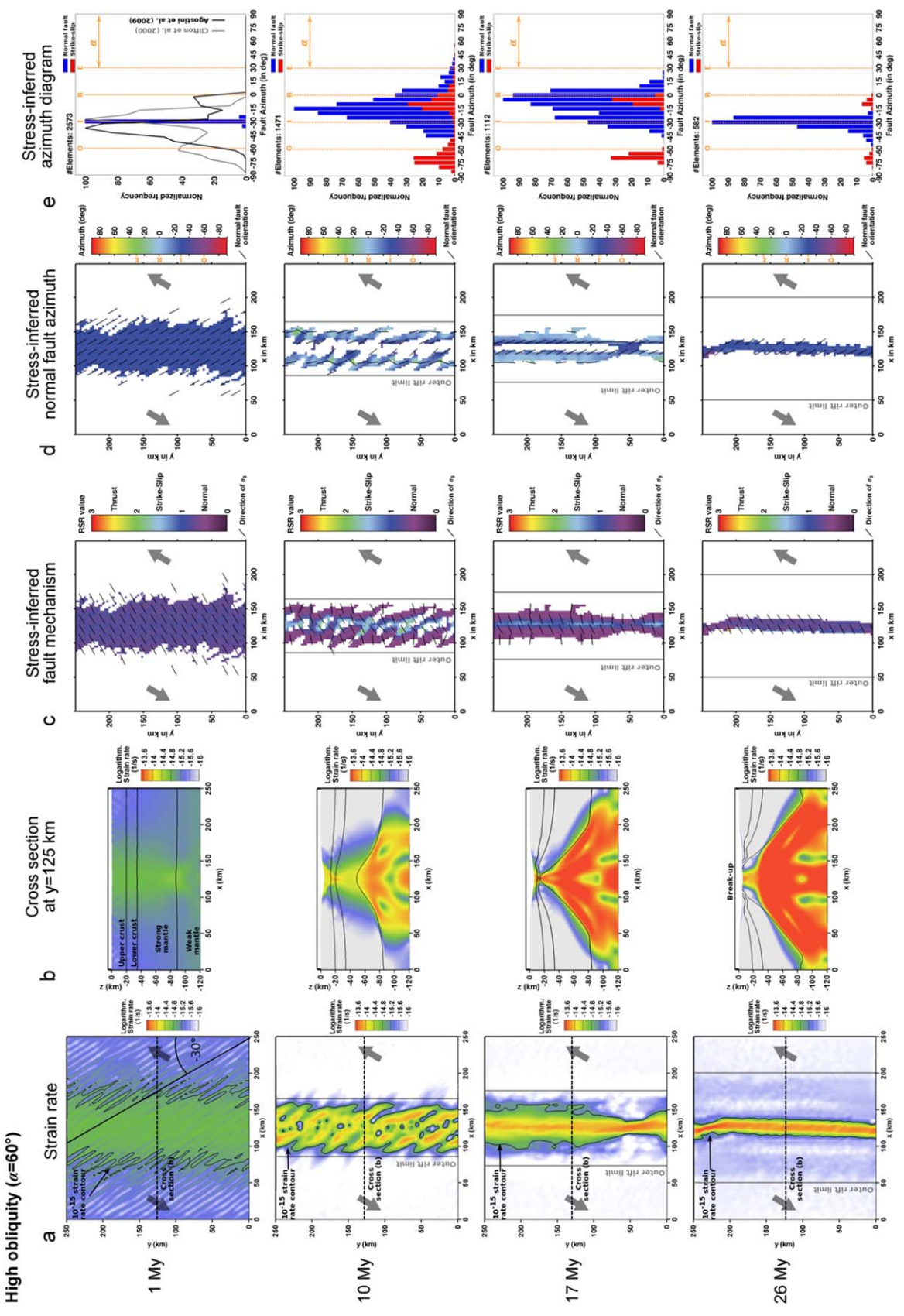

Figure 8. High obliquity ($\alpha = 60°$). (a) At 1 My, shear zones are parallel to the expected intermediate shear zone azimuth of $-30°$. (b) Cross section showing the degree of lithospheric necking (c) An initially transtensional stress regime gives way to a strike-slip zone in the rift center (10 and 17 My) and a normal fault domain adjacent to the rift center (strain partitioning). (d, e) Normal fault azimuths rotate from intermediate to rift-parallel while lithospheric necking takes place as seen in Figure 8b. Rift-parallel faulting ends abruptly during basinward localization, followed by intermediate fault directions. Abbreviations are explained in the caption of Figure 4. For a detailed model evolution in 2 My time steps, see supporting information animation A5.

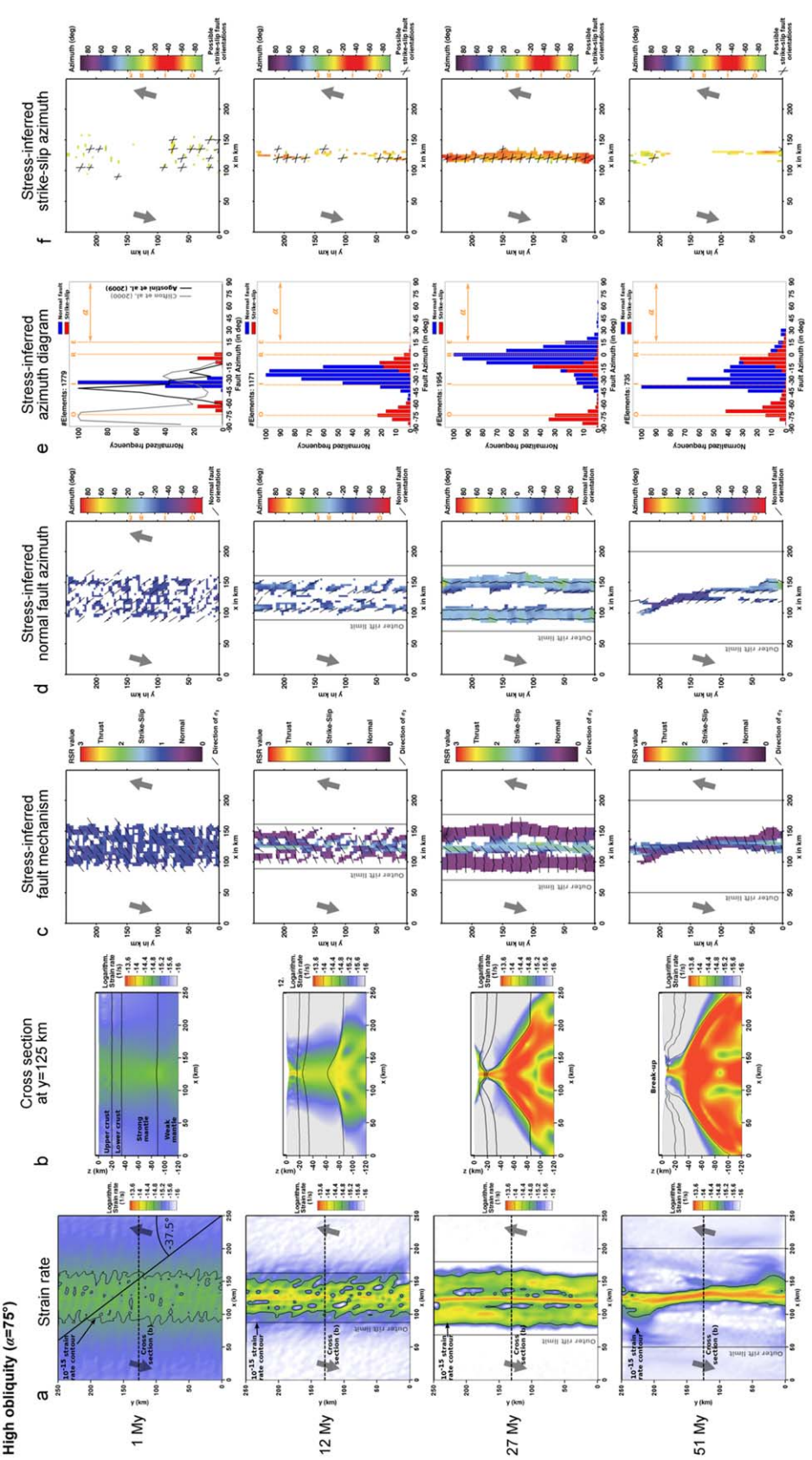

Figure 9. High obliquity ($\alpha = 75°$). (a) Diffuse shear zones are visible in the strain rate images. (b) Cross section showing the degree of lithospheric necking. (c, d, e) Strong strain partitioning occurs between rift center (strike-slip faults) and rift boundary (rift-parallel normal faults). Normal fault directions change from intermediate (1 My) to rift parallel (27 My) and back to intermediate (51 My). In contrast to previous figures, a Figure 9f exists that shows strike-slip azimuths. These are plotted as doublets which accounts for the impossibility to distinguish between sinistral and dextral faults based on stress-tensor information alone. Abbreviations are explained in the caption of Figure 4. For a detailed model evolution in 3 My time steps, see supporting information animation A6.

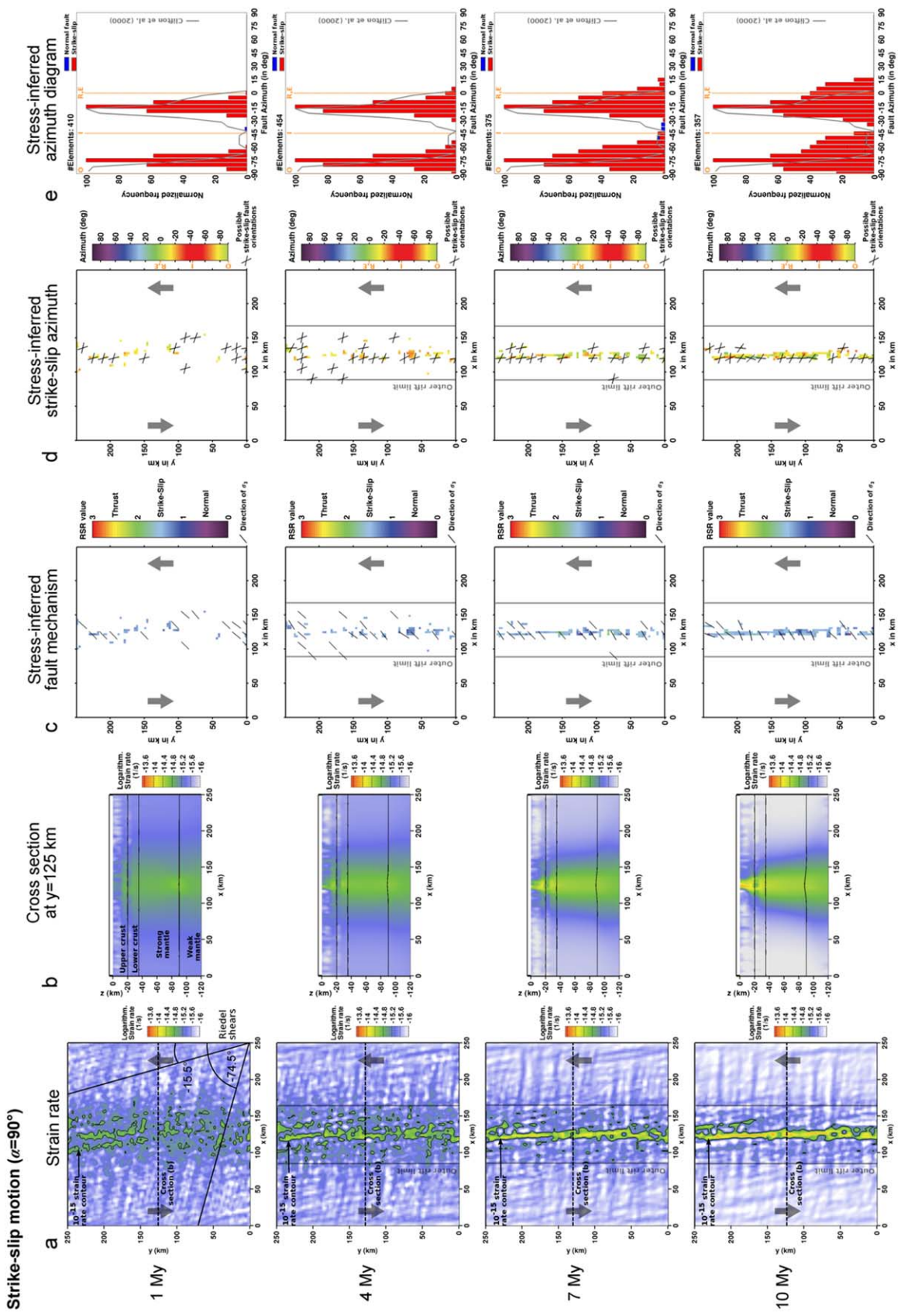

Figure 10. Strike-slip deformation ($\alpha = 90°$). (a) Two fault families are visible corresponding to synthetic and antithetic Riedel shears. (b) Cross sections show localization into a central strike-slip fault and its ductile continuation into lower crust and mantle. (c, d, e) Stress-inferred fault orientations throughout the experiment. In contrast to previous figures, plot (d) shows strike-slip fault azimuths, since normal faults do not exist. Abbreviations are explained in the caption of Figure 4. For a detailed model evolution in 1 My time steps, see supporting information animation A7.

3.1. General Behavior

During the first million years of extension, small-scale shear zones emerge spontaneously over the entire model width. They compete due to frictional softening until they coalesce into few dominant shear zones in the center of the model atop the lithospheric necking zone. These shear zones form a distinct en-échelon pattern in all models with oblique rift direction, whereby their overall number increases with obliquity. Note that the model resolution of 3 km does not allow to reproduce faults in a strict sense; however, finite-width shear zones with a typical width of several elements can be observed.

With continuing deformation, the central portion of the en-échelon shear zones appears to rotate counterclockwise with a vertical axis so that the shear zones develop a sigmoidal shape. The rotation is caused by the longevity of the shear zones [*Brune and Autin*, 2013]: Oblique rifting transforms long-lived shear zones via stretching which appears as a rotation. Due to basinward localization, shear zones at the rift margin become inactive at an early stage and hence accommodate less rotation than shear zones in the rift center which continue rotating until they are almost parallel to extension.

The normal faults that emerge from the initial phase of coalescence rotate to smaller dip with continued extension. When they reach a dip angle of approximately 30°, they become inactive and new, basinward located faults commence to accommodate brittle strain. In all model runs except the strike-slip end member, successive localization toward the rift center generates a graben-in-graben structure. The transition during an individual localization event can be very rapid (i.e., faster than 1 My), especially for a mature rift close to breakup.

Since the applied modeling approach does not account for the formation of oceanic crust, continental breakup is reached when the crust is broken and asthenospheric material reaches the surface. The required time to reach breakup grows with increased rift obliquity since the overall extension rate is kept constant for all setups so that the rift-perpendicular extension velocity is smaller for larger obliquity. For the case of $\alpha=90°$, it is zero and no breakup takes place at all.

3.2. Orthogonal Rifting ($\alpha=0$)

Initial deformation is distributed over the whole model (Figure 4a). Within 6 My, however, successive coalescence of small-scale shear zones leads to the emergence of distinct rift segments with a small offset in-between. There are two offset locations (at $y = 120-170$ km and $y = 0-30$ km). Each rift segment is bounded by a set of conjugate normal faults that cut through the whole crust and lead to Moho uplift (Figure 4b). With continued deformation, new basinward dipping normal faults localize close to the rift center until crustal breakup takes place at 11 My.

The stress regime (Figure 4c) is purely extensional during the whole experiment. This can also be seen for individual stress components and the nearly constant RSR value at the center of the model (Figure 3). The azimuth distribution shows more complexity than expected for an essentially 2-D setup (Figure 4d). This is caused by the formation of the aforementioned two rift segments. Within each segment, normal faults strike in y direction with 0° azimuth but at the offsets, the principal stress direction of σ_3 rotates smoothly so that the inferred normal fault azimuth reaches 70° and −70°, respectively.

The azimuth diagrams (Figure 4e) mirror the structural evolution of the system. The initial structures at 1 My with homogeneous 0° azimuth evolve into a widened distribution. At 6 My, the rift offsets contribute a small number of elements with azimuths of ±70°. When the rift segments merge into a single rift zone at 8 My, the azimuth distribution narrows again to 0° until breakup at 11 My.

3.3. Low Obliquity ($\alpha=15°, 30°$)

At 1 My, the strain rate patterns of Figures 5a and 6a show small-scale shear zones that strike at an angle of −7.5° and −15°, respectively, that is exactly the intermediate azimuth of the extension-orthogonal direction and the rift orientation. Throughout this paper, I refer to this specific direction as "intermediate" fault orientation. At 5–6 My, along-strike segmentation of the rift is depicted in the strain rate plots that are characterized by en-échelon shear zone patterns. Successive localization toward the rift center ends the en-échelon deformation and leads to crustal breakup along a straight ridge.

The stress-inferred fault mechanism (Figures 5c and 6c) is of normal type at the beginning, followed by some minor strike-slip deformation in the rift center before finally returning to pure extension. Fault

azimuths develop in four phases (Figures 5d and 6d): (i) The coalescence phase involves intermediate directions. (ii) During en-échelon deformation, individual segments are connected by fault populations with diverse orientation of 0–70°. In contrast to the orthogonal setup with α=0°, the fault azimuth distribution is skewed toward higher values, which compensates the obliquity of the individual en-échelon shear zones. Some strike-slip faulting occurs with conjugate fault azimuths of 5° and −55° in the $\alpha = 30°$ scenario (Figure 6e). (iii) Lithospheric necking unites the rift segments prior to breakup and homogenizes normal fault azimuths to mainly intermediate directions. (iv) Breakup entails both extension-orthogonal and intermediate normal fault orientations.

3.4. Moderate Obliquity (α=45°)

In many structural aspects, the model with 45° obliquity shows a mixture between the low and the high-obliquity experiments. The coalescence phase starts with intermediately oriented fault azimuths (Figures 7a, 7d, and 7e) that develop into an en-échelon system at 6 My. Similar to the low-obliquity models, the en-échelon segments are connected at the rift boundaries with smoothly varying fault orientations that exceed the rift-parallel azimuth of 0°. In contrast to the low-obliquity models, however, rift-parallel faults adjacent to the rift center are much more pronounced (Figures 7d and 7e at 11 My). They emerge at the end of the en-échelon deformation when strong lithospheric necking occurs below the central part of the rift. Simultaneously, a thin, strike-slip dominated area emerges in the rift center and vanishes again upon crustal breakup. The latest stages of rifting show intermediate fault orientations while additional extension-orthogonal fault azimuths appear during breakup.

3.5. High Obliquity (α=60°, 75°)

The high-obliquity models are governed both by normal faulting and strike-slip deformation. Initial small-scale shear zones feature normal fault characteristics and strike with intermediate direction across the rift (Figures 8a and 9a). For α=60°, the initial RSR value indicates an extensional/transtensional stress regime (Figure 8c). For the rift center, a detailed evolution of the stress regime is depicted in Figure 3 illustrating the transition from extensional to strike-slip and back to extensional in terms of individual stress components. The α=75° model features a transtensional/strike-slip stress regime from the beginning of rifting (Figure 9c). Individual en-échelon segments exist for the 60° scenario at 10 My, while for 75° they are hardly distinguishable at 12 My.

With continuing deformation, a pronounced strike-slip zone emerges in the rift center of both models. For α=75°, the stress-inferred orientation of strike-slip faults is displayed in Figures 9e and 9f. The coexistence of strike-slip and normal faults indicates strain partitioning between the strike-slip dominated rift center and the surrounding normal fault system. Nevertheless, the period of rift-parallel faulting at the rift flanks coincides also with strong lithospheric necking and hence strong lateral density gradients, whereas both strain partitioning and lateral density gradients enhance rift-parallel faulting.

The two high-obliquity models differ during the breakup stage. For α=60°, lithospheric necking focuses the region of deformation prior to breakup until the central strike-slip region is replaced by intermediately oriented normal faults. For 75° obliquity, however, strike-slip faults persist before and after breakup.

3.6. Strike-Slip Deformation (α=90°)

As expected, the model with α=90° is entirely dominated by strike-slip faults. Synthetic and antithetic Riedel shears are visible in Figure 10a, oriented at $-\varphi_{eff}/2 = -15.5°$ and $-90° + \varphi_{eff}/2 = -74.5°$, respectively. (The effective friction angle φ_{eff} is 31° according to an effective friction coefficient μ of 0.6.). A single large shear zone with strike-slip characteristics (Figure 10c) localizes in the center of the model that continues into lower crustal portions and upper mantle as a single ductile shear zone (Figure 10b). An evaluation of the stress-inferred strike-slip azimuth yields again Riedel shear orientations. Note that the two strike-slip families in Figure 10e are due to the impossibility to discriminate between the two conjugate strike-slip fault orientations based on stress information only. This is also the reason for the symmetry in the color scale with respect to the direction of σ_1 (−45°) in Figure 10d.

3.7. Model Robustness and Limitations

Several alternative model runs have been conducted in order to test the influence of key parameters such as lower crustal rheology, extension velocity, model resolution, and the strain rate threshold of the stress-interpretation method. The resulting evolution of fault orientations is depicted for all angles of obliquity in supporting information Figures S1–S5. Even though some of these models differ in terms of timing, the characteristic evolution of fault patterns remains identical to the standard scenario displayed in Figure 11.

Due to the simplicity of the shown models, there are several limitations that should be considered when comparing the presented results to natural rift environments. Most importantly, inherited structures affect stress and localization pattern such that faults might align along preexisting faults and not with optimal orientation. Moreover, neither melting and magma migration nor subsequent dyke formation are taken into account and surface processes like erosion and sedimentation are omitted.

The limits of computational power impose severe constraints on the overall number of numerical elements. In this study, I use 83 × 83 × 40 elements resulting in a model-wide resolution of 3 km. Only when more efficient solvers and adaptive mesh refinement techniques become available, will numerical lithospheric-scale models be able to directly resolve small-scale fault systems in three dimensions.

Three-dimensional variations in density and viscosity generate a stress field that can be vertically heterogeneous. By inferring a fault azimuth from the surface stress tensor, the model assumes that the generation of new faults is controlled by the shallow stress regime. This means that information about the model's stress structure at depth is discarded here, leaving room for future improvements of the stress visualization technique.

Mid-oceanic ridges with fast and intermediate spreading velocities are dominated by a characteristic zig-zag pattern of extension-orthogonal ridges and extension-parallel transforms. These fault orientations are not expressed in the strain rate pattern of the numerical model that produces a single straight ridge oblique to extensional direction. The reason is that the 10 mm/yr full extension velocity of the numerical model is typical for ultraslow spreading ridges that extend with a rate less than 12 mm/yr [*Dick et al*., 2003]. Slow and ultraslow spreading ridges often feature oblique extension with intermediate fault populations [*Tuckwell et al*., 1996; *Fournier and Petit*, 2007], which agrees very well with the stress-inferred fault patterns in the final phase after breakup.

4. Comparison to Analog Experiments

In this section, numerical results are compared to two sets of analog experiments, namely *Clifton et al*. [2000], and *Agostini et al*. [2009]. To my knowledge, these models constitute the latest crustal-scale and lithospheric-scale sets of experiments, respectively, that cover a large spectrum of obliquity (i.e., $0^\circ \leq \alpha \leq 90^\circ$ in *Clifton et al*. [2000], and $0^\circ \leq \alpha \leq 75^\circ$ in *Agostini et al*. [2009]). There are significant differences between the setup of *Clifton et al*. [2000] and the numerical model in terms of rheology, model dimensions, and total extension while only two major differences exist with the analog model of *Agostini et al*. [2009]; the implementation of the weak zone, and the boundary conditions, whereas dimensions and rheology are very similar. Nevertheless, it is especially the difference between the individual setups that allows relevant conclusions: Fault patterns that are robustly reproduced by both the analog experiments and the numerical model can be expected to represent fundamental features that should be visible in nature as well.

The experiments of *Clifton et al*. [2000] involve a single layer of clay which is considered as the laboratory analog of a crustal layer that is deformed without any interaction with the underlying mantle. According to their scaling, 1 cm in the model corresponds to roughly 0.1–1 km in nature. Hence their quadratic model setup with a length of 60 cm scales to 6–60 km in reality, while the thickness of the clay layer scales to 0.25–2.5 km. Fault orientations are measured at a scaled displacement of 0.6–6 km. The prospective rift zone is prescribed by a latex sheet at the bottom of the box whose width scales to 0.6–6 km. The definition of α in the original publication is opposite to the one applied here ($\alpha = 90^\circ - \alpha_{\mathrm{Clifton}}$). Since the clay-model allows only crust-scale deformation, the maximum total strain is only 10%, which corresponds to 2.5 My of extension in the numerical model. The final fault distribution of *Clifton et al*. [2000] is depicted at 1 My in Figures 4e–10e as a gray line.

The laboratory experiments of *Agostini et al*. [2009] are conducted using a complex layered setup that involves brittle rheology in the upper crust, a ductile lower crust, as well as lithospheric and asthenospheric mantle layers following *Corti* [2008]. The lithosphere-asthenosphere boundary lies at 42 km depth (2.8 cm in model dimension). The brittle upper crust is represented by K-feldspar powder while the depth-dependent viscosity of lower crust and mantle is realized by several layers composed of plasticine-silicone mixtures. Lateral model dimensions scale to 240 km times 180–270 km, while maximum extension is 42 km. A prescribed rift zone of 45 km width is introduced via a weak lower crustal domain. A major difference between *Agostini et al*. [2009]

and the numerical model exists in terms of the boundary condition. The analog model involves free-slip boundary conditions at the nonextending model sides imposing zero shear stress along these boundaries. The numerical setup features a periodic boundary condition that is best illustrated by an infinite concatenation of the model domain along the rift trend. Moreover, their imposed weak zone lies oblique to the model boundaries, so that it partially coincides with the extensional boundary for $\alpha > 45°$. Note that the fault distribution of *Agostini et al.* [2009] has been measured after 23% total strain which corresponds to 58 km (i.e., 5.8 My) in the numerical experiments. Their resulting fault distribution is shown in Figures 4e–10e as a black line. The coordinate system of *Agostini et al.* [2009] differs from this study, so that for comparability, the fault distribution had to be adopted to the numerical model configuration.

The following subsections compare numerical and analog experiments in terms of individual fault populations in more detail. However, comparison is limited to the first stages of rifting, since final stages and breakup are not covered by analog models.

4.1. Faults with Intermediate Direction

Faults with intermediate direction (i.e., orientations between displacement-orthogonal and rift-parallel orientation) constitute the fundamental mode of faulting and are present in all experiments on oblique extension. They result from the orientation of the principal stress axes with respect to the rift zone [*Withjack and Jamison*, 1986] in accordance with Andersonian faulting. The faults cross the whole rift zone in *Clifton et al.* [2000] and in the first time steps of the numerical model. During lithospheric necking, the rift structure of the numerical model is dominated by major, basinward dipping boundary faults that organize in en-échelon shear zones, reproducing the structures observed by *Agostini et al.* [2009]. Strong agreement exists in terms of the small-scale surface structures of the rift boundary that consists of intermediately oriented faults. In both *Agostini et al.* [2009] and in the numerical model, basinward localization generates internal faults and graben-in-graben structures [*Corti et al.*, 2010].

However, intermediate faults are restricted in *Agostini et al.* [2009] to the rift margins while they develop in the numerical model throughout the rift valley. The reason possibly lies in different implementations of the weak zone: The analog models feature a sharp, rheological transition from normal to weak lower crust focusing reorientation of local extension to the boundaries of the weak zone. The numerical models, however, involve a gradual, thermal transition between the weak zone and normal crust without a focusing effect. Another possible explanation is that the numerical model's weak zone is stronger than in the analog models which leads to more crust-mantle coupling and a narrower rift [*Buck*, 1991] that cannot accommodate the central horst seen in the analog models.

4.2. Displacement-Orthogonal Faulting

This fault population occurs in the analog experiments of both *Clifton et al.* [2000] and *Agostini et al.* [2009] albeit in a different manner. It is found for high obliquity ($\alpha \geq 60°$) in the experiments of *Clifton et al.* [2000], while in the setup of *Agostini et al.* [2009] it takes place only at moderate to low obliquity ($\alpha \leq 45°$) and is manifested as internal faults. In the numerical model, displacement-orthogonal faults emerge at moderate to low obliquity ($\alpha \leq 45°$). However, they are less important than in the analog models and emerge only at a very late rift stage reminiscent of the typical zig-zag mid-ocean ridge pattern of transform and extension-perpendicular deformation.

Displacement-orthogonal faults are generated when the local stress field is not affected by oblique structures. A homogeneous, isotropic material that is stretched in any direction will always show displacement-orthogonal faulting. An alternative reason for the occurrence of displacement-orthogonal faulting is a free-slip boundary condition which does not support any shear stress so that faults tend to be perpendicular to that side of the model.

One reason for sparsity of displacement-orthogonal faults in the numerical model is the periodic boundary condition that is less prone to displacement-orthogonal faulting than the free-slip boundary condition of the analog models. Another reason could be the low numerical resolution (if compared to analog models) that hampers the evolution of individual rift segments and segmented mid-ocean ridges [*Gerya*, 2013]. Additionally, the analog model's strong viscosity contrast between weak zone and normal crust induces a sharp local stress reorientation and thereby possibly generates a rift interior that is dominated by extension-orthogonal stresses.

4.3. Rift Parallel Faulting

Rift parallel faulting is present in the numerical model and the analog model of *Agostini et al.* [2009], but not in the crustal-scale experiments of *Clifton et al.* [2000], which suggests that lithospheric necking is controlling the occurrence of this fault family. Even though rift-parallel faulting takes place in the numerical model and in *Agostini et al.* [2009], they are generated by a different mechanism: In the analog experiments, these fault orientations occur for $\alpha \geq 30^\circ$ as strike-slip or oblique-slip faults at the area of minimum lithospheric thinning. They are secondary structures that connect two distinct extension-perpendicular segments in the center of the rift. In the numerical model, however, they occur much later, toward the end of the en-échelon phase (Figure 11) as a result of lithospheric necking.

Lithospheric necking may generate rift-parallel faulting by two means: (i) The density contrast of hot upwelling material below the rift center and the cold continental mantle lithosphere beneath the rift flanks generates a rift-perpendicular stress-component [*Sonder*, 1990; *Bellahsen et al.*, 2006, 2013]. (ii) An additional factor enhancing rift-parallel faulting is strain partitioning. Strike-slip faults emerge at the weakest point of the rift, i.e., above the necking maximum. These strike-slip faults partially account for the rift-parallel component of the far-field extension velocity while normal faulting at the rift flanks accommodates the rift-orthogonal component [*Brune and Autin*, 2013].

4.4. Strike-Slip Faulting

Strike-slip faults play a major role for intermediate and high obliquity in the analog models and the numerical experiments. For $\alpha = 45^\circ - 75^\circ$, both the model of *Agostini et al.* [2009] and the numerical experiments exhibit a strong strike-slip zone with fault orientations subparallel to the rift trend. This strike-slip-dominated area locates in the rift center where lithospheric thinning resulted in maximum weakening. In the numerical model, rift-centered strike-slip faults occur simultaneously with rift-parallel fault orientations adjacent to the rift center indicating strain partitioning.

The numerical model of simple shear ($\alpha = 90^\circ$) features strike-slip faults with two populations whose respective orientations are both subparallel to the rift trend and the direction of extension. These direction are associated with Riedel shear orientations that exhibit characteristic azimuths of $-\varphi_{\text{eff}}/2 = -15.5^\circ$ and $\varphi_{\text{eff}}/2 - 90^\circ = -74.5^\circ$. These angles are visible both in the strain rate pattern (Figure 10a) as well as in the stress-inferred fault azimuth (Figure 10d and 10e). The experiment with $\alpha = 90^\circ$ compares very well to the corresponding model of *Clifton et al.* [2000]. However, the analog model displays only the sinistral fault family, while the dextral population seems to be shifted to the extension-normal orientation.

5. Discussion and Comparison to Selected Natural Examples

The presented numerical models show how the surface stress field in an oblique rift system varies significantly during different phases of rifting, even though the extension rate and direction remain constant. The underlying reason for this behavior is the interaction of far-field stresses with rift-intrinsic buoyancy and strength. This result agrees with previous field-based studies that infer local stress rotations in the Baikal Rift [*Petit et al.*, 1996], the western branch of the East African Rift System [*Morley*, 2010], and the Main Ethiopian Rift [*Corti et al.*, 2013]. The inference of rift-intrinsic, time-dependent variations of fault orientation complicates the approach to deduce palaeostress field and associated plate motion changes based on fault orientations of rift systems.

Strain partitioning has been recognized as an important process during transtension and transpression [*Teyssier et al.*, 1995]. The numerical model indicates that strain partitioning between strike-slip in the rift center and adjacent rift-parallel normal faulting occurs for high rift obliquity. The reason for this behavior is that strike-slip deformation is more pronounced for high obliquities, as expected from infinitesimal strain theory [*Withjack and Jamison*, 1986]. While strike-slip faults account for a certain portion of the along-strike velocity component, the rift-perpendicular component generates normal faults that feature rift-parallel azimuths. The model shows strain-partitioning at the end of the en-échelon deformation. It might therefore explain the rift-parallel faults observed in the Gulf of Aden [*Bellahsen et al.*, 2006]. Note that strain-partitioning occurs in a different manner than in previous analog models [*Agostini et al.*, 2009], where boundary faults at the rift margin deform via oblique slip whereas the rift center shows pure extension.

Moreover, strain-partitioning occurs in their models for low obliquity ($\alpha<45°$) and not for highly oblique extension.

Strike-slip localization due to strain partitioning affects the rift process also in terms of mechanical energy. Since strike-slip motion requires less force (at constant velocity) than oblique extension [*Brune et al*., 2012], a strike-slip zone in the rift center will significantly facilitate the rift process.

Comparison to a previous numerical model of oblique extension [*van Wijk*, 2005] yields basic agreement but also significant differences. Similar to analog models [*Agostini et al*., 2009; *Autin et al*., 2010], this study prescribes a weak linear zone that is oblique to the model boundaries and uses the free-slip condition at lateral boundaries. Maximum model extension is ~120 km achieving crustal thinning factors of 1.2 so that break-up does not occur. Similar to the results presented here, *van Wijk* [2005] reports shear zones that cut across the inherited weak zone; however, these shear zones exhibit only extension-orthogonal strike whereas no intermediate directions are visible. A reason for the dominant extension-orthogonal orientation could be the free-slip boundary condition that prohibits shear stress at the model sides. This contrasts the periodic boundary condition of the models presented here that imposes less influence on shear zone orientation.

Oblique extensional systems worldwide differ in many aspects and clearly one single model cannot explain all rifts at the same time. However, the distinct fault populations occurring in the presented numerical model and their sequence of activity can elucidate observations from different rift systems.

The model with $\alpha=45°$ compares very well to the evolution of the Gulf of Aden featuring an obliquity of about 40° [see *Brune and Autin*, 2013 for a detailed discussion]. The succession of fault populations of the Gulf of Aden displays a three-phase chronology consistent of (i) initially intermediate and extension-orthogonal faulting, (ii) followed by rift-parallel azimuths, and (iii) a final phase of intermediate faults that have been found at the ocean-continent boundary and extension-orthogonal faults adjacent to the ridge [*Bellahsen et al*., 2013]. This fault evolution corresponds very well to the phases of the numerical model presented here. Large displacement-orthogonal basins that exist on-shore [*Leroy et al*., 2012] do not match the numerical model. These basins, however, correspond to areas of Mesozoic extension that have been reactivated during Gulf of Aden rift activity [*Ellis et al*., 1996; *Leroy et al*., 2012; *Autin et al*., 2013].

The curved Main Ethiopian Rift is characterized by ~30° obliquity in the central sector and ~45° in the northern sector [*Corti*, 2009]. Fault analysis shows a two phase evolution. At first, boundary faults developed with intermediate orientation along an area of significant strength contrast between the inherited weak zone and the surrounding strong lithosphere. The second phase is marked by strain migration to the rift center where en-échelon faulting takes place with extension-orthogonal azimuths [*Corti*, 2008]. The numerical model reproduces the major boundary faults and their small-scale structure that is dominated by intermediate fault directions. Basinward strain localization like in the Main Ethiopian rift takes place in the numerical model and is caused by lithospheric necking explaining the observed two-phase evolution. En-échelon faults develop in the numerical model and in the central parts of the Main Ethiopian Rift; however, instead of rift-parallel fault populations, the latter shows extension-orthogonal fault directions. This difference might originate from the geometry of the weak zone and its actual strength, both of which are submitted to the paramount influence of the Afar plume [*Ebinger and Sleep*, 1998].

The Gulf of California region constitutes a rift system that features high obliquity of $\alpha=60°-70°$. The tectonic setting is very complex and derives from an active margin featuring strong lateral density variations and an inherited belt of weak crust from a volcanic arc [*Umhoefer*, 2011]. Additional complexity arises from a possible two-phase evolution involving an orthogonal and an oblique phase of extension [*Stock and Hodges*, 1989]. Hence, any attempt to understand the Gulf of California by means of a simple model must be taken with due caution. Nevertheless, several structural aspects of this rift system can be related to the presented model. Counterclockwise rotation of long-lived shear zones in the numerical model (sinistral oblique rifting) corresponds to clockwise rotation when translated to the Gulf of California extensional configuration (dextral oblique rifting). These clockwise vertical-axis block rotations of fault systems have been interpreted in the northeastern part of Baja California [*Seiler et al*., 2010; *Bennett and Oskin*, 2014]. Moreover, strong rift-parallel faulting like in the numerical model has been inferred during the proto-Gulf phase of rifting [*Stock and Hodges*, 1989]. Strain partitioning has been interpreted during the formation of the proto-Gulf [*Stock and Hodges*, 1989; *Oskin and Stock*, 2003] with dextral strike-slip west of the peninsula (i.e., outside the rift) and rift-parallel normal faulting within

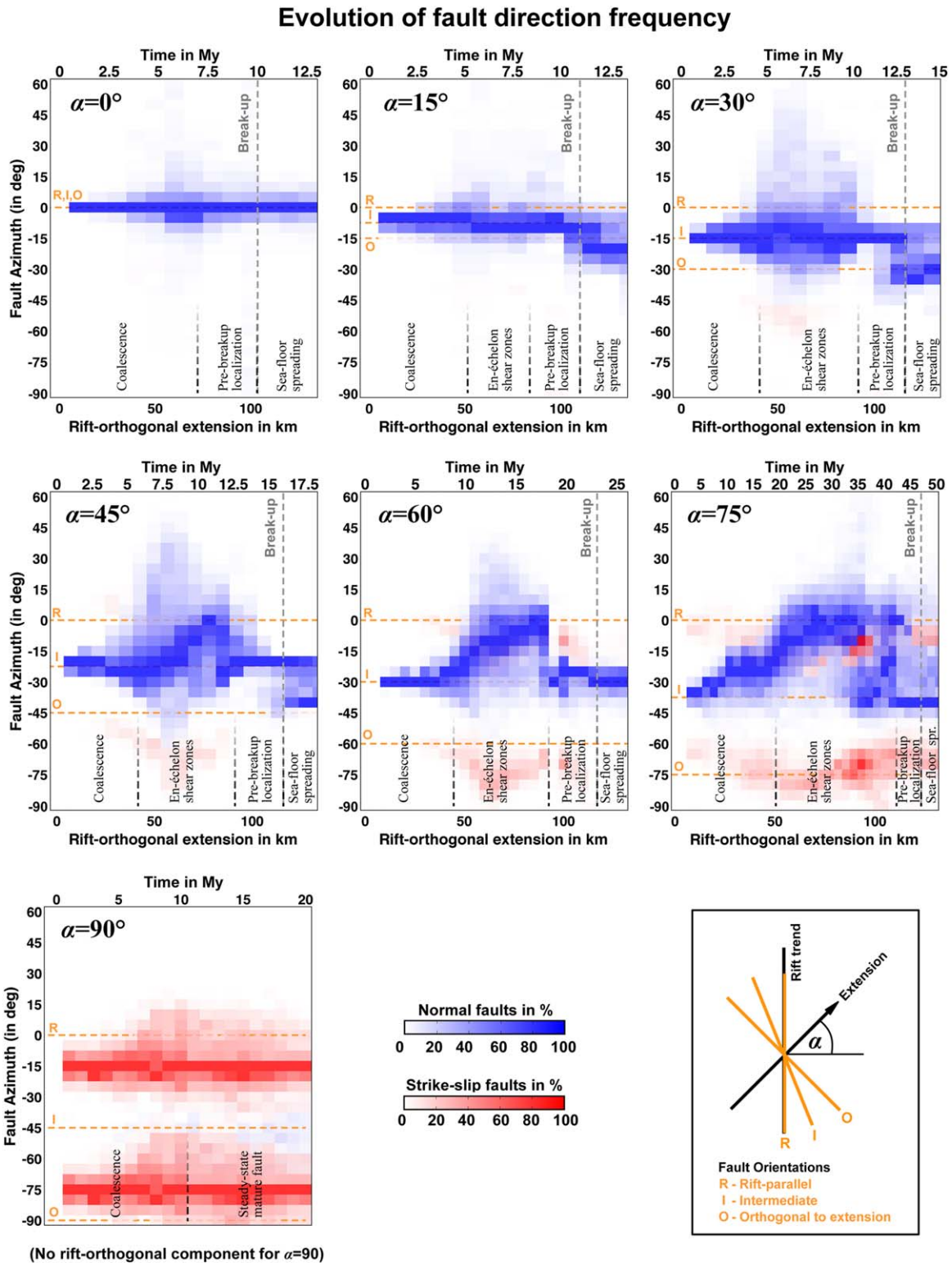

Figure 11. Summary plot. Azimuth diagrams shown in previous plots (Figures 4e–10e) are condensed into one plot for each angle of obliquity. This illustrates the evolution of normal faults (blue) and strike-slip faults (red) in distinct phases. The abscissa shows rift-orthogonal extension (bottom axis) and time (top axis). Breakup is indicated by a gray dashed line. Initially dominating intermediate fault directions (I) widen during fault coalescence and shift toward rift-parallel azimuths (R) during a phase of en-échelon deformation. Prebreakup localization towards the rift center ends the en-échelon phase within few million years and homogenizes fault orientations to intermediate directions. Post breakup sea floor spreading takes place with intermediate and extension-orthogonal faults (O) for $\alpha \leq 45^\circ$ while only intermediate directions exist for $\alpha = 60^\circ$ and $\alpha = 75^\circ$. For obvious reasons, the model without obliquity ($\alpha = 0^\circ$) and the strike-slip model ($\alpha = 90^\circ$) do not feature an en-échelon phase. The strike-slip model ($\alpha = 90^\circ$) exhibits a stage of fault maturity, but no break-up. The robustness of the presented models is illustrated in supporting information Figures S1–S5, where important model parameters are varied.

the rift, a result that is currently discussed [*Fletcher et al*., 2007; *Seiler et al*., 2010]. The presented high-obliquity numerical scenarios indicate a certain degree of strain partitioning. However, in the numerical models, the strike-slip zone occurs inside the rift center and not adjacent to the rift valley.

Even though the model was designed to understand continental rift systems, it can be very well applied to oblique oceanic extensional systems. These have been characterized by en-échelon graben patterns and intermediate fault orientations that are very similar to those of the presented models. Prominent examples are the Reykjanes and Mohns ridges [*Dauteuil and Brun*, 1993], the Viking graben [*Brun and Tron*, 1993], the Sogn graben [*Faerseth et al*., 1997], and the Southwest Indian Ridge [*Montési et al*., 2011].

6. Conclusions

The presented rift models generate complex time-dependent surface structures despite the fact that the setup is fairly simple. The only reason for this complexity is the intrinsic three-dimensionality of oblique rift systems. Other mechanisms such as surface processes, reactivation of inherited structures, melting, and dyke dynamics provide additional complexity for the tectonic evolution of individual rift systems.

The evolution of the inferred surface fault orientations is summarized for all angles of obliquity in Figure 11. Individual models can be described in four phases that mirror the structural evolution of the rift:

1. Initial fault coalescence with intermediate fault directions results from interaction of the far field stress with the obliquely oriented weak zone.

2. En-échelon deformation featuring a broad distribution of fault orientations occurs whereas rift-parallel faults gain successively more importance. Rift-parallel faults are favored both by necking-induced density variations and strain partitioning between strike-slip in the rift center and normal fault in its vicinity.

3. Prebreakup localization rapidly terminates the en-échelon phase yielding intermediate fault orientations.

4. Sea floor spreading involves intermediate and extension-orthogonal fault directions as a result of the waning influence of the inherited oblique weakness.

While fault directions are often used to infer palaeoplate movements, this study shows that local variations in crustal stress field and fault orientation may arise intrinsically during rift maturation and may not require plate motion changes. The evolution of crustal stress and fault directions follow a characteristic temporal pattern that is linked to the maturity of the rift system.

Acknowledgments

S. B. has been funded by SAMPLE (South Atlantic Margin Processes and Links with onshore Evolution), Priority Program 1375 of the German Research Foundation and by the European Research Council, through the Marie Curie International Outgoing Fellowship (Project 326115). I thank the reviewers, Giacomo Corti, Patrice Rey, and an anonymous reviewer for their detailed and constructive comments. This study benefited greatly from discussions with Oliver Heidbach, Julia Autin, Andrey Babeyko, and Jonathan Bull. Stephan Sobolev and Dietmar Müller are thanked for support. Furthermore, I thank Simon Williams for giving feedback on the manuscript.

References

Agostini, A., G. Corti, A. Zeoli, and G. Mulugeta (2009), Evolution, pattern, and partitioning of deformation during oblique continental rifting: Inferences from lithospheric-scale centrifuge models, *Geochem. Geophys. Geosyst.*, *10*, Q11015, doi:10.1029/2009GC002676.

Agostini, S., C. Doglioni, F. Innocenti, P. Manetti, and S. Tonarini (2010), On the geodynamics of the Aegean rift, *Tectonophysics*, *488*, 7–21, doi:10.1016/j.tecto.2009.07.025.

Allken, V., R. S. Huismans, and C. Thieulot (2011), Three-dimensional numerical modeling of upper crustal extensional systems, *J. Geophys. Res.*, *116*, B10409, doi:201110.1029/2011JB008319.

Allken, V., R. S. Huismans, and C. Thieulot (2012), Factors controlling the mode of rift interaction in brittle-ductile coupled systems: A 3D numerical study, *Geochem. Geophys. Geosyst.*, *13*, Q05010, doi:10.1029/2012GC004077.

Anderson, E. M. (1948), *The Dynamics of Faulting*, Oliver and Boyd, Edinburgh.

Autin, J., N. Bellahsen, L. Husson, M.-O. Beslier, S. Leroy, and E. d' Acremont (2010), Analog models of oblique rifting in a cold lithosphere, *Tectonics*, *29*, TC6016, doi:10.1029/2010TC002671.

Autin, J., N. Bellahsen, S. Leroy, L. Husson, M.-O. Beslier, and E. d' Acremont (2013), The role of structural inheritance in oblique rifting: Insights from analogue models and application to the Gulf of Aden, *Tectonophysics*, *607*, 51–64, doi:10.1016/j.tecto.2013.05.041.

Bassi, G. (1991), Factors controlling the style of continental rifting: Insights from numerical modelling, *Earth Planet. Sci. Lett.*, *105*, 430–452, doi:10.1016/0012–821X(91)90183-I.

Behn, M. D., J. Lin, and M. T. Zuber (2002), A continuum mechanics model for normal faulting using a strain-rate softening rheology: Implications for thermal and rheological controls on continental and oceanic rifting, *Earth Planet. Sci. Lett.*, *202*, 725–740, doi:10.1016/S0012-821X(02)00792-6.

Bellahsen, N., C. Faccenna, F. Funiciello, J. M. Daniel, and L. Jolivet (2003), Why did Arabia separate from Africa? Insights from 3-D laboratory experiments, *Earth Planet. Sci. Lett.*, *216*, 365–381, doi:10.1016/S0012-821X(03)00516-8.

Bellahsen, N., M. Fournier, E. d' Acremont, S. Leroy, and J. M. Daniel (2006), Fault reactivation and rift localization: Northeastern Gulf of Aden margin, *Tectonics*, *25*, TC1007, doi:10.1029/2004TC001626.

Bellahsen, N., L. Husson, J. Autin, S. Leroy, and E. d' Acremont (2013), The effect of thermal weakening and buoyancy forces on rift localization: Field evidences from the Gulf of Aden oblique rifting, *Tectonophysics*, *607*, 80–97, doi:10.1016/j.tecto.2013.05.042.

Bennett, S. E. K., and M. E. Oskin (2014), Oblique rifting ruptures continents: Example from the Gulf of California shear zone, *Geology*, *42*(3), 215–218, doi:10.1130/G34904.1.

Bialas, R.W., and W. R. Buck (2009), How sediment promotes narrow rifting: Application to the Gulf of California, *Tectonics*, *28*, TC4014, doi:10.1029/2008TC002394.

Bonini, M., T. Souriot, M. Boccaletti, J. P. Brun (1997), Successive orthogonal and oblique extension episodes in a rift zone: Laboratory experiments with application to the Ethiopian Rift, *Tectonics*, *16*, 347–362, doi:10.1029/96TC03935.

Bott, M. H. P. (1959), The mechanics of oblique slip faulting, *Geol. Mag.*, *96*, 109–117.

Braun, J., and C. Beaumont (1989), A physical explanation of the relation between flank uplifts and the breakup unconformity at rifted continental margins, *Geology*, *17*, 760–764, doi:10.1130/0091-7613(1989)017<0760:APEOTR>2.3.CO;2.

Brun, J.-P., and V. Tron (1993), Development of the North Viking Graben: Inferences from laboratory modelling, *Sediment. Geol.*, *86*, 31–51, doi:10.1016/0037-0738(93)90132-O.

Brune, S., and J. Autin (2013), The rift to break-up evolution of the Gulf of Aden: Insights from 3D numerical lithospheric-scale modelling, *Tectonophysics*, *607*, 65–79, doi:10.1016/j.tecto.2013.06.029.

Brune, S., A. A. Popov, and S. V. Sobolev (2012), Modeling suggests that oblique extension facilitates rifting and continental break-up, *J. Geophys. Res.*, *117*, B08402, doi:10.1029/2011JB008860.

Brune, S., A. A. Popov, and S. V. Sobolev (2013), Quantifying the thermo-mechanical impact of plume arrival on continental break-up, *Tectonophysics*, *604*, 51–59, doi:10.1016/j.tecto.2013.02.009.

Brune, S., C. Heine, M. Perez-Gussinye, and S. V. Sobolev (2014), Rift migration explains continental margin asymmetry and crustal hyperextension, *Nat. Commun. 5*, 4014, doi:10.1038/ncomms5014.

Buchmann, T. J., and P. T. Connolly (2007), Contemporary kinematics of the Upper Rhine Graben: A 3D finite element approach, *Global Planet. Change*, *58*, 287–309, doi:10.1016/j.gloplacha.2007.02.012.

Buck, W. R. (1991), Modes of continental lithospheric extension, *J. Geophys. Res.*, *96*, 20161–20178, doi:10.1029/91JB01485.

Buck, W. R. (2006), The role of magma in the development of the Afro-Arabian Rift System, *Geol. Soc. Spec. Publ.*, *259*, 43–54, doi:10.1144/GSL.SP.2006.259.01.05.

Buiter, S. J. H., R. S. Huismans, and C. Beaumont (2008), Dissipation analysis as a guide to mode selection during crustal extension and implications for the styles of sedimentary basins, *J. Geophys. Res.*, *113*, B06406, doi:10.1029/2007JB005272.

Burov, E., and S. Cloetingh (1997), Erosion and rift dynamics: New thermomechanical aspects of post-rift evolution of extensional basins, *Earth Planet. Sci. Lett.*, *150*, 7–26, doi:10.1016/S0012-821X(97)00069-1.

Choi, E., and W. R. Buck (2012), Constraints on the strength of faults from the geometry of rider blocks in continental and oceanic core complexes, *J. Geophys. Res.*, *117*, B04410, doi:10.1029/2011JB008741.

Chorowicz, J., and C. Sorlien (1992), Oblique extensional tectonics in the Malawi Rift, Africa, *Geol. Soc. Am. Bull.*, *104*, 1015–1023, doi:10.1130/0016-7606(1992)104<1015:OETITM>2.3.CO;2.

Clifton, A. E., R. W. Schlische, M. O. Withjack, and R. V. Ackermann (2000), Influence of rift obliquity on fault-population systematics: Results of experimental clay models, *J. Struct. Geol.*, *22*, 1491–1509, doi:10.1016/S0191–8141(00)00043-2.

Corti, G. (2008), Control of rift obliquity on the evolution and segmentation of the main Ethiopian rift, *Nat. Geosci.*, *1*, 258–262, doi:10.1038/ngeo160.

Corti, G. (2009), Continental rift evolution: From rift initiation to incipient break-up in the Main Ethiopian Rift, East Africa, *Earth Sci. Rev.*, *96*, 1–53, doi:10.1016/j.earscirev.2009.06.005.

Corti, G. (2012), Evolution and characteristics of continental rifting: Analog modeling-inspired view and comparison with examples from the East African Rift System, *Tectonophysics*, *522–523*, 1–33, doi:10.1016/j.tecto.2011.06.010.

Corti, G., M. Bonini, F. Innocenti, P. Manetti, and G. Mulugeta (2001), Centrifuge models simulating magma emplacement during oblique rifting, *J. Geodyn.*, *31*, 557–576, doi:10.1016/S0264–3707(01)00032-1.

Corti, G., M. Bonini, S. Conticelli, F. Innocenti, P. Manetti, and D. Sokoutis (2003), Analogue modelling of continental extension: A review focused on the relations between the patterns of deformation and the presence of magma, *Earth Sci. Rev.*, *63*, 169–247, doi:10.1016/S0012-8252(03)00035-7.

Corti, G., G. Ranalli, G. Mulugeta, A. Agostini, F. Sani, and A. Zugu (2010), Control of the rheological structure of the lithosphere on the inward migration of tectonic activity during continental rifting, *Tectonophysics*, *490*, 165–172, doi:10.1016/j.tecto.2010.05.004.

Corti, G., M. Philippon, F. Sani, D. Keir, and T. Kidane (2013), Re-orientation of the extension direction and pure extensional faulting at oblique rift margins: Comparison between the Main Ethiopian Rift and laboratory experiments, *Terra Nova*, *25*, 396–404, doi:10.1111/ter.12049.

Dauteuil, O., and J. P. Brun (1993), Oblique rifting in a slow-spreading ridge, *Nature*, *361*, 145–148, doi:10.1038/361145a0.

De Wit, M. J. (2003), Madagascar: Heads it's a continent, tails it's an Island, *Annu. Rev. Earth Planet. Sci.*, *31*, 213–248, doi:10.1146/annurev.earth.31.100901.141337.

Delvaux, D., R. Moeys, G. Stapel, C. Petit, K. Levi, A. Miroshnichenko, V. Ruzhich, and V. San'kov (1997), Paleostress reconstructions and geodynamics of the Baikal region, Central Asia, Part 2. Cenozoic rifting, *Tectonophysics*, *282*, 1–38, doi:10.1016/S0040-1951(97)00210-2.

Dick, H. J. B., J. Lin, and H. Schouten (2003), An ultraslow-spreading class of ocean ridge, *Nature*, *426*, 405–412, doi:10.1038/nature02128.

Dorsey, R. J. (2010), Sedimentation and crustal recycling along an active oblique-rift margin: Salton Trough and northern Gulf of California, *Geology*, *38*, 443–446. doi:10.1130/G30698.1.

Dunbar, J. A., and D. S. Sawyer (1996), Three-dimensional dynamical model of continental rift propagation and margin plateau formation, *J. Geophys. Res.*, *101*, 27845–27,863, doi:10.1029/96JB01231.

Ebinger, C. J., and N. H. Sleep (1998), Cenozoic magmatism throughout east Africa resulting from impact of a single plume, *Nature*, *395*, 788–791, doi:10.1038/27417.

Ellis, A. C., H. M. Kerr, C. P. Cornwell, and D. O. Williams (1996), A tectono-stratigraphic framework for Yemen and its implications for hydrocarbon potential, *Pet. Geosci.*, *2*, 29–42, doi:10.1144/petgeo.2.1.29.

Engen, Ø., J. I. Faleide, and T. K. Dyreng (2008), Opening of the Fram Strait gateway: A review of plate tectonic constraints, *Tectonophysics*, *450*, 51–69, doi:10.1016/j.tecto.2008.01.002.

England, P., and D. McKenzie (1982), A thin viscous sheet model for continental deformation, *Geophys. J. R. Astron. Soc.*, *70*, 295–321, doi:10.1111/j.1365-246X.1982.tb04969.x.

Faerseth, R.B., B.-E. Knudsen, T. Liljedahl, P. S. Midbøe, and S. Søderstrøm (1997), Oblique rifting and sequential faulting in the Jurassic development of the northern North Sea, *J. Struct. Geol.*, *19*, 1285–1302, doi:10.1016/S0191-8141(97)00045-X.

Fletcher, J. M., M. Grove, D. Kimbrough, O. Lovera, and g. E. Gehrels (2007), Ridge-trench interactions and the Neogene tectonic evolution of the Magdalena shelf and southern Gulf of California: Insights from detrital zircon U-Pb ages from the Magdalena fan and adjacent areas, *Geol. Soc. Am. Bull.*, *119*, 1313–1336, doi:10.1130/B26067.1.

Fournier, M., and C. Petit (2007), Oblique rifting at oceanic ridges: Relationship between spreading and stretching directions from earthquake focal mechanisms, *J. Struct. Geol.*, *29*, 201–208, doi:10.1016/j.jsg.2006.07.017.
Gac, S., and L. Geoffroy (2009), 3D Thermo-mechanical modelling of a stretched continental lithosphere containing localized low-viscosity anomalies (the soft-point theory of plate break-up), *Tectonophysics*, *468*, 158–168, doi:10.1016/j.tecto.2008.05.011.
Gaina, C., R. D. Müller, B. Brown, T. Ishihara, and S. Ivanov (2007), Breakup and early seafloor spreading between India and Antarctica, *Geophys. J. Int.*, *170*, 151–169, doi:10.1111/j.1365-246X.2007.03450.x.
Gerya, T. (2010), Dynamical instability produces transform faults at mid-ocean ridges, *Science*, *329*, 1047–1050, doi:10.1126/science.1191349.
Gerya, T.V. (2013), Three-dimensional thermomechanical modeling of oceanic spreading initiation and evolution, *Phys. Earth Planet. Inter. 214*, *35–52*, doi:10.1016/j.pepi.2012.10.007.
Gleason, G. C., and J. Tullis (1995), A flow law for dislocation creep of quartz aggregates determined with the molten-salt cell, *Tectonophysics*, *247*, 1–23.
Heine, C., and S. Brune (2014), Oblique rifting of the equatorial Atlantic: Why there is no Saharan Atlantic Ocean, *Geology 42(3)*, *211–214*, doi:10.1130/G35082.1.
Hergert, T., and O. Heidbach (2011), Geomechanical model of the Marmara Sea region—II. 3-D contemporary background stress field, *Geophys. J. Int.*, *185*, 1090–1102, doi:10.1111/j.1365-246X.2011.04992.x.
Hirth, G., and D. L. Kohlstedt (2003), Rheology of the upper mantle and the mantle wedge: A view from the experimentalists, in Inside the Subduction Factory, Geophys. Monogr. Ser. vol. 138, edited by J. M. Eiler, pp. 83–105, AGU, Washington, D. C., doi:10.1029/138GM06.
Hosseinpour, M., R. D. Müller, S. E. Williams, and J. M. Whittaker (2013), Full-fit reconstruction of the Labrador Sea and Baffin Bay, *Solid Earth*, *4*, 461–479, doi:10.5194/se-4-461-2013.
Houseman, G., and P. England (1986), Finite strain calculations of continental deformation: 1. Method and general results for convergent zones, *J. Geophys. Res.*, *91*, 3651–3663, doi:10.1029/JB091iB03p03651.
Huismans, R. S., and C. Beaumont (2003), Symmetric and asymmetric lithospheric extension: Relative effects of frictional-plastic and viscous strain softening, *J. Geophys. Res.*, *108*(B10), 2496, doi:10.1029/2002JB002026.
Huismans, R. S., and C. Beaumont (2011), Depth-dependent extension, two-stage breakup and cratonic underplating at rifted margins, *Nature*, *473*, 74–78, doi:10.1038/nature09988.
Katzman, R., U. S. ten Brink, and J. Lin (1995), Three-dimensional modeling of pull-apart basins: Implications for the tectonics of the Dead Sea Basin, *J. Geophys. Res.*, *100*, 6295–6312, doi:10.1029/94JB03101.
Lavier, L. L., and G. Manatschal (2006), A mechanism to thin the continental lithosphere at magma-poor margins, *Nature*, *440*, 324–328, doi:10.1038/nature04608.
Lavier, L. L., W. R. Buck, and A. N. B. Poliakov (2000), Factors controlling normal fault offset in an ideal brittle layer, *J. Geophys. Res.*, *105*, 23431–23,442, doi:10.1029/2000JB900108.
Le Pourhiet, L., B. Huet, D. A. May, L. Labrousse, and L. Jolivet (2012), Kinematic interpretation of the 3D shapes of metamorphic core complexes, *Geochem. Geophys. Geosyst.*, *13*, Q09002, doi:10.1029/2012GC004271.
Le Pourhiet, L., B. Huet, and N. Traore (2014), Links between long-term and short-term rheology of the lithosphere: Insights from strike-slip fault modelling, *Tectonophysics*, doi:10.1016/j.tecto.2014.06.034, in press.
Leroy, S., et al. (2012), From rifting to oceanic spreading in the Gulf of Aden: A synthesis, *Arab. J. Geosci.*, *5*, 859–901, doi:10.1007/s12517-011-0475-4.
Liao, J., and T. Gerya (2014), Influence of lithospheric mantle stratification on craton extension: Insight from two-dimensional thermo-mechanical modeling, *Tectonophysics*, in press, doi:10.1016/j.tecto.2014.01.020.
Lizarralde, D., et al. (2007), Variation in styles of rifting in the Gulf of California, *Nature*, *448*, 466–469, doi:10.1038/nature06035.
Mart, Y., and O. Dauteuil (2000), Analogue experiments of propagation of oblique rifts, *Tectonophysics*, *316*, 121–132, doi:10.1016/S0040-1951(99)00231-0.
McClay, K. R., and M. J. White (1995), Analogue modelling of orthogonal and oblique rifting, *Mar. Pet. Geol.*, *12*, 137–151, doi:10.1016/0264-8172(95)92835-K.
Montési, L. G. J., M. D. Behn, L. B. Hebert, J. Lin, and J. L. Barry (2011), Controls on melt migration and extraction at the ultraslow Southwest Indian Ridge 10°–16°E, *J. Geophys. Res.*, *116*, B10102, doi:10.1029/2011JB008259.
Morley, C. K. (2010), Stress re-orientation along zones of weak fabrics in rifts: An explanation for pure extension in ''oblique'' rift segments?, *Earth Planet. Sci. Lett.*, *297*, 667–673, doi:10.1016/j.epsl.2010.07.022.
Moulin, M., D. Aslanian, and P. Unternehr (2010), A new starting point for the South and Equatorial Atlantic Ocean, *Earth Sci. Rev.*, *98*, 1–37, doi:10.1016/j.earscirev.2009.08.001.
Nürnberg, D., and R. D. Müller (1991), The tectonic evolution of the South-Atlantic from Late Jurassic to present, *Tectonophysics*, *191*, 27–53, doi:10.1016/0040–1951(91)90231-G.
Oskin, M., and J. Stock (2003), Pacific–North America plate motion and opening of the Upper Delfín basin, northern Gulf of California, Mexico, *Geol. Soc. Am. Bull.*, *115*, 1173–1190, doi:10.1130/B25154.1.
Pérez-Gussinyé, M., J. P. Morgan, T. J. Reston, and C. R. Ranero (2006), The rift to drift transition at non-volcanic margins: Insights from numerical modelling, *Earth Planet. Sci. Lett.*, *244*, 458–473, doi:10.1016/j.epsl.2006.01.059.
Petersen, K. D., S. B. Nielsen, O. R. Clausen, R. Stephenson, and T. Gerya (2010), Small-scale mantle convection produces stratigraphic sequences in sedimentary basins, *Science*, *329*, 827–830, doi:10.1126/science.1190115.
Petit, C., J. Déverchère, F. Houdry, V. A. Sankov, V. I. Melnikova, and D. Delvaux (1996), Present-day stress field changes along the Baikal rift and tectonic implications, *Tectonics*, *15*, 1171–1191, doi:10.1029/96TC00624.
Popov, A. A., and S. V. Sobolev (2008), SLIM3D: A tool for three-dimensional thermo mechanical modeling of lithospheric deformation with elasto-visco-plastic rheology, *Phys. Earth Planet. Inter. 171*, 55–75, doi:10.1016/j.pepi.2008.03.007.
Provost, A.-S., and H. Houston (2003), Stress orientations in northern and central California: Evidence for the evolution of frictional strength along the San Andreas plate boundary system, *J. Geophys. Res.*, *108*(B3), 2175, doi:10.1029/2001JB001123.
Regenauer-Lieb, K., R. F. Weinberg, and G. Rosenbaum (2006), The effect of energy feedbacks on continental strength, *Nature*, *442*, 67–70, doi:10.1038/nature04868.
Rey, P. F., and G. Houseman (2006), Lithospheric scale gravitational flow: The impact of body forces on orogenic processes from Archaean to Phanerozoic, *Geol. Soc. Spec. Publ.*, *253*, 153–167, doi:10.1144/GSL.SP.2006.253.01.08.
Rey, P. F., C. Teyssier, S. C. Kruckenberg, and D. L. Whitney (2011), Viscous collision in channel explains double domes in metamorphic core complexes, *Geology*, *39*, 387–390, doi:10.1130/G31587.1.
Ring, U. (1994), The influence of preexisting structure on the evolution of the Cenozoic Malawi rift (East African rift system), *Tectonics*, *13*, 313–326, doi:10.1029/93TC03188.

Rooney, T. O., I. D. Bastow, D. Keir, F. Mazzarini, E. Movsesian, E. B. Grosfils, J. R. Zimbelman, M. S. Ramsey, D. Ayalew, and G. Yirgu (2014), The protracted development of focused magmatic intrusion during continental rifting, *Tectonics*, *33*, 875–897, doi:10.1002/2013TC003514.

Seiler, C., J. M. Fletcher, M. C. Quigley, A. J. W. Gleadow, and B. P. Kohn (2010), Neogene structural evolution of the Sierra San Felipe, Baja California: Evidence for proto-gulf transtension in the Gulf Extensional Province?, *Tectonophysics*, *488*, 87–109, doi:16/j.tecto.2009.09.026.

Simpson, R. W. (1997), Quantifying Anderson's fault types, *J. Geophys. Res.*, *102*, 17,909–17,919, doi:199710.1029/97JB01274.

Smith, M., and P. Mosley (1993), Crustal heterogeneity and basement influence on the development of the Kenya Rift, East Africa, *Tectonics*, *12*, 591–606, doi:10.1029/92TC01710.

Sokoutis, D., G. Corti, M. Bonini, J. P. Brun, S. Cloetingh, T. Mauduit, and P. Manetti (2007), Modelling the extension of heterogeneous hot lithosphere, *Tectonophysics*, *444*, 63–79, doi:10.1016/j.tecto.2007.08.012.

Sonder, L. J. (1990), Effects of density contrasts on the orientation of stresses in the lithosphere: Relation to principal stress directions in the Transverse Ranges, California, *Tectonics*, *9*, 761–771, doi:10.1029/TC009i004p00761.

Stock, J. M., and K. V. Hodges (1989), Pre-Pliocene Extension around the Gulf of California and the transfer of Baja California to the Pacific Plate, *Tectonics*, *8*, 99–115, doi:10.1029/TC008i001p00099.

Storey, M., J. J. Mahoney, A. D. Saunders, R. A. Duncan, S. P. Kelley, and M. F. Coffin (1995), Timing of Hot Spot—Related Volcanism and the Breakup of Madagascar and India, *Science*, *267*, 852–855, doi:10.1126/science.267.5199.852.

Strecker, M. R., P. M. Blisniuk, and G. H. Eisbacher (1990), Rotation of extension direction in the central Kenya Rift, *Geology*, *18*, 299–302, doi:10.1130/0091-7613(1990)018<0299:ROEDIT>2.3.CO;2.

Suckro, S. K., K. Gohl, T. Funck, I. Heyde, A. Ehrhardt, B. Schreckenberger, J. Gerlings, V. Damm, and W. Jokat (2012), The crustal structure of southern Baffin Bay: Implications from a seismic refraction experiment, *Geophys. J. Int.*, *190*(1), 37–58, doi:10.1111/j.1365-246X.2012.05477.x.

Teyssier, C., B. Tikoff, and M. Markley (1995), Oblique plate motion and continental tectonics, *Geology*, *23*, 447–450, doi:10.1130/0091–7613(1995)023<0447:OPMACT>2.3.CO;2.

Torsvik, T. H., S. Rousse, C. Labails, M. A. Smethurst (2009), A new scheme for the opening of the South Atlantic Ocean and the dissection of an Aptian salt basin, *Geophys. J. Int.*, *177*, 1315–1333, doi:10.1111/j.1365-246X.2010.04727.x.

Tron, V., and J.-P. Brun (1991), Experiments on oblique rifting in brittle-ductile systems, *Tectonophysics*, *188*, 71–84, doi:10.1016/0040–1951(91)90315-J.

Tuckwell, G. W., J. M. Bull, and D. J. Sanderson (1996), Models of fracture orientation at oblique spreading centres, *J. Geol. Soc.*, *153*, 185–189, doi:10.1144/gsjgs.153.2.0185.

Umhoefer, P. J. (2011), Why did the Southern Gulf of California rupture so rapidly?—Oblique divergence across hot, weak lithosphere along a tectonically active margin, *GSA Today*, *21*(11), 4–10, doi:10.1130/G133A.1.

Van Wijk, J. W. (2005), Role of weak zone orientation in continental lithosphere extension, *Geophys. Res. Lett.*, *32*, L02303, doi:10.1029/2004GL022192.

Van Wijk, J. W., and D. K. Blackman (2005), Dynamics of continental rift propagation: The end-member modes, *Earth Planet. Sci. Lett.*, *229*, 247–258, doi:10.1016/j.epsl.2004.10.039.

Van Wijk, J. W., and S. A. P. L. Cloetingh (2002), Basin migration caused by slow lithospheric extension, *Earth Planet. Sci. Lett.*, *198*, 275–288, doi:10.1016/S0012–821X(02)00560-5.

Whittaker, J. M., R. D. Müller, G. Leitchenkov, H. Stagg, M. Sdrolias, C. Gaina, and A. Goncharov (2007), Major Australian-Antarctic plate reorganization at Hawaiian-Emperor bend time, *Science 318*, *83–86*, doi:10.1126/science.1143769.

Wilks, K. R., and N. L. Carter (1990), Rheology of some continental lower crustal rocks, *Tectonophysics*, *182*, 57–77, doi:10.1016/0040–1951(90)90342-6.

Williams, S. E., J. M. Whittaker, and R. D. Müller (2011), Full-fit, palinspastic reconstruction of the conjugate Australian-Antarctic margins, *Tectonics*, *30*, TC6012, doi:201110.1029/2011TC002912.

Withjack, M. O., and W. R. Jamison (1986), Deformation produced by oblique rifting, *Tectonophysics*, *126*, 99–124, doi:10.1016/0040–1951(86)90222-2.

Zoback, M. D., et al. (1987), New evidence on the state of stress of the San Andreas fault system, *Science 238*, 1105–1111, doi:10.1126/science.238.4830.1105.

Zuber, M. T., and E. M. Parmentier (1986), Lithospheric necking: A dynamic model for rift morphology, *Earth Planet. Sci. Lett.*, *77*, 373–383, doi:10.1016/0012-821X(86)90147-0.